A. P. Alexandrov
RESEARCH INSTITUTE
OF TECHNOLOGY
N I T I

Investigation of corium melt interaction with NPP reactor vessel steel (METCOR-P)

Progress report 1/04/08-30/06/08

INVESTIGATION OF CORIUM MELT INTERACTION WITH NPP REACTOR VESSEL STEEL IN AN INERT ABOVE-MELT ATMOSPHERE WITH VERTICAL POSITIONING OF THE INTERACTION INTERFACE

EXPERIMENT MCP-1

Project title	Investigation of Corium Melt Interaction with NPP Reactor Vessel Steel (METCOR-P) No. 3592	
Contracting organization	ISTC	
File code	RMP-01	
Project location	Alexandrov Research Institute of Technology of the RF Agency for Atomic Energy. NITI, Sosnovy Bor, 188540 Leningrad Region, Russia	
Project manager	Name	V.B. Khabensky
	Signature	
	Date	30 June 2008

Authors

Dr.(Eng.), Prof.	V. B. Khabensky
Dr.(Eng.)	S. V. Bechta
Ph.D.	V. S. Granovsky
Ph.D.	A. A. Sulatsky
	S. A. Vitol
	E. V. Krushinov
Ph.D.	S. Yu. Kotova
Academician	V. V. Gusarov
Ph.D.	I. V. Kulagin
Ph.D.	D. B. Lopukh
	V. I. Almjashev
	E.M. Belyaeva
	V. G. Bliznyuk
	V. R. Bulygin
	E. K. Kalyago
	N. E. Kamensky
	R.A. Kosarevsky
	A. V. Lysenko
	A. P. Martynov
	V. V. Martynov
	E. V. Shevchenko
	A. A. Chertkov
Ph.D.	S. A. Smirnov

ABSTRACT

The report presents a description and results of MCP-1 test of the METCOR-P ISTC Project carried out in the NITI, Sosnovy Bor, on the "Rasplav-3" test facility.

The interaction of vessel steel with molten corium ~C-32 (as per charge) with vertical positioning of the specimen and maximum ~1400ºC on its surface has been studied in an inert atmosphere (argon).

CONTENTS

Introduction

The interaction of molten suboxidized UO_2-ZrO_2-Zr corium with vessel steel was experimentally investigated in MC6-MC9 tests of the METCOR Project with horizontal positioning of the interaction interface. Under conditions of a VVER severe accident with formation of a molten pool on the vessel cooled bottom, the interaction interface inclination may be within the 0…90° range, i.e. vary from horizontal to vertical. A possible influence of this parameter on the process of interaction required an additional investigation.

In accordance with the METCOR-P Work Plan, the conditions realized in MCP-1 (vertical positioning of the interface) were as close as possible to those in MC6, with the maximum temperature on the steel specimen surface in the MC6-MC9 experimental series and the minimum corium oxidation index. The test was aimed at determining qualitative and quantitative characteristics of interaction and their comparison with the corresponding characteristics in MC6.

1. TEST DESCRIPTION

1.1. Experimental facility diagram

The induction system of the Rasplav-3 facility has been modernized to enable performing tests with vertical positioning of the vessel steel specimen. Prior to the main test, Pr2-MCP-1 pretest has been performed to check reliability of the vessel steel specimen cooling system, and Pr1-MCP-1 – for synthesizing C-32 corium (the main charge material) in order to reduce height of the charge in the crucible in the main test. Besides, a preliminary numerical modeling of the molten pool thermal hydraulics has been performed and a diagram of thermocouples location in the specimen developed. The results of experimental investigations and calculations allowed designing and producing an experimental cell together with the system of its cooling and screening.

Diagram of the furnace from MCP-1 is given in Fig. 1.1. The vessel steel specimen represented a cylinder Ø 28 mm and 60 mm high, with a coaxial cooling channel Ø 3 mm. The crucible with welded sections was used for screening the lower cooling water discharge branch pipe (Fig. 1.1). The cylindrical specimen was positioned along the crucible axis and rested on the bottom calorimeter. The calorimeter top was 10 mm above the welded sections top. A water-cooled shaft screen was placed above the specimen to ensure screening of the top cooling water inlet branch pipe. Specimen cooling employs an individual circuit with a pressure-increasing pump. To observe the melt surface, the furnace cover has two viewing ports covered with quartz windows. Fig. 1.2 and Tab. 1.1 offer the locations of thermocouples. K-type thermocouples were placed in through holes Ø 1.5 mm except for Nos. TC03, TC11, for which the holes were drilled in the specimen bottom end to a depth of thermocouples embedding.

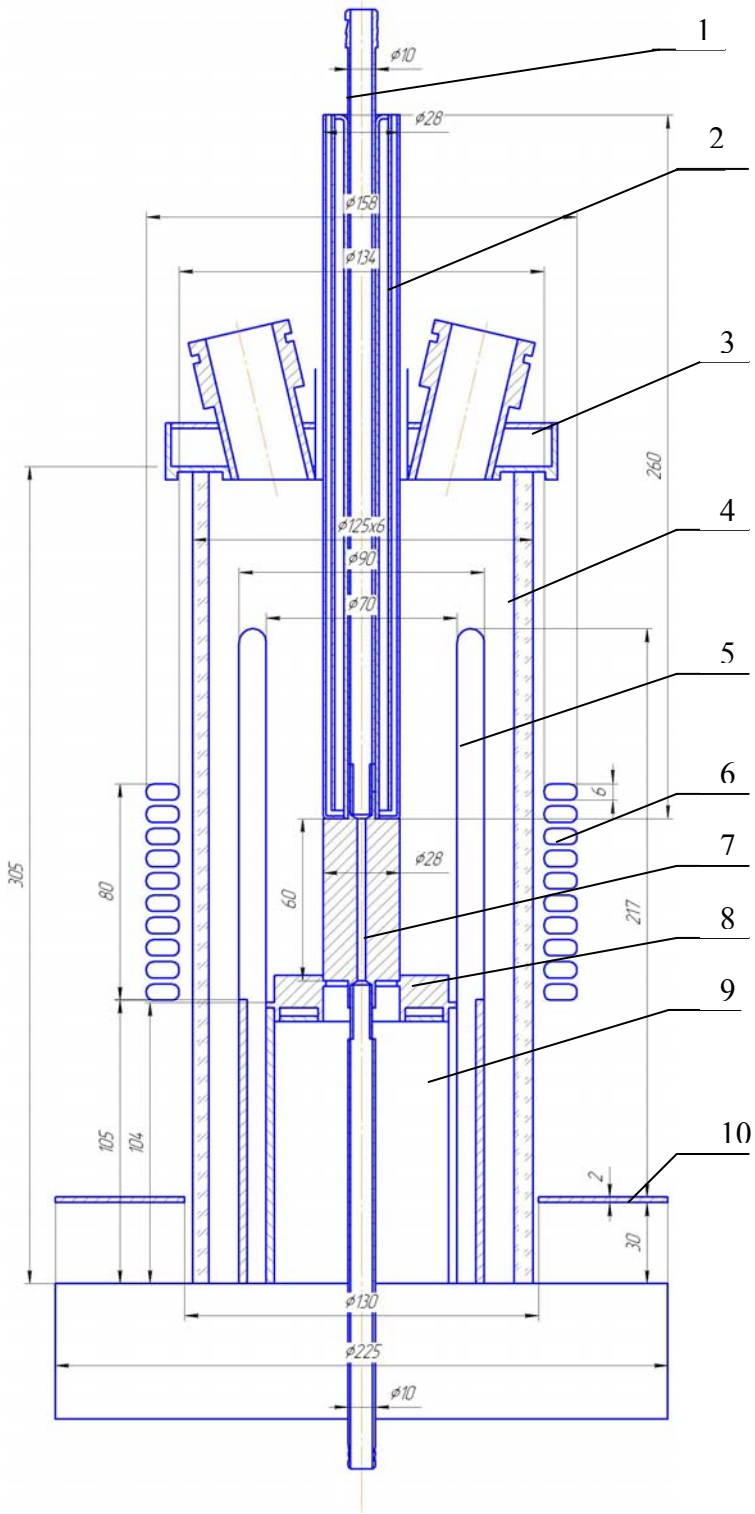

1 – specimen cooling branch pipe, 2 water-cooled shaft screen, 3 – water-cooled cover, 4 – quartz tube, 5 – crucible section, 6 – inductor, 7 – vessel steel specimen, 8 – bottom calorimeter, 9 – calorimeter support, 10 – non-cooled screen.

Fig. 1.1 – Furnace diagram

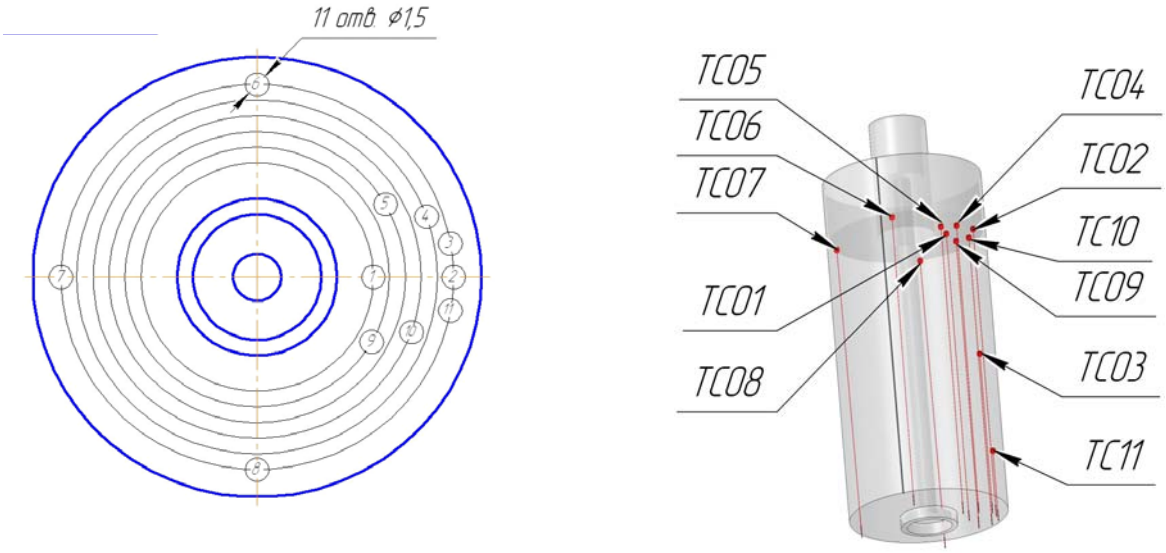

Fig. 1.2 – Thermocouple hot junction locations

Table 1.1

Thermocouple hot junction locations

No.	**h, mm** (distance from the specimen bottom end to the hot junction)	**Θ,°** (horizontal angle)	**r, mm** (distance from the specimen axis to the hot junction)
1	50	0	7.25
2	50	0	12.25
3	27	10	12.25
4	50	20	11.25
5	50	30	9.25
6	50	90	12.25
7	50	180	12.25
8	50	270	12.25
9	50	330	8.25
10	50	340	10.25
11	11	350	12.25

The gas-aerosol system is presented in Fig. 1.3. High-purity argon was used for maintaining inert atmosphere in the furnace (1). The atmosphere was controlled using the electrochemical oxygen sensor (7). During the test, the furnace was overpressured with argon. The Petryanov Medium Area Filter was used for aerosol sampling (5). To control the gas flow parameters (pressure and temperature), Motorola pressure transducers and L-type thermocouples were installed in places marked by dots in the diagram. A silica gel column (2) was applied for removing moisture traces from gas at the furnace inlet.

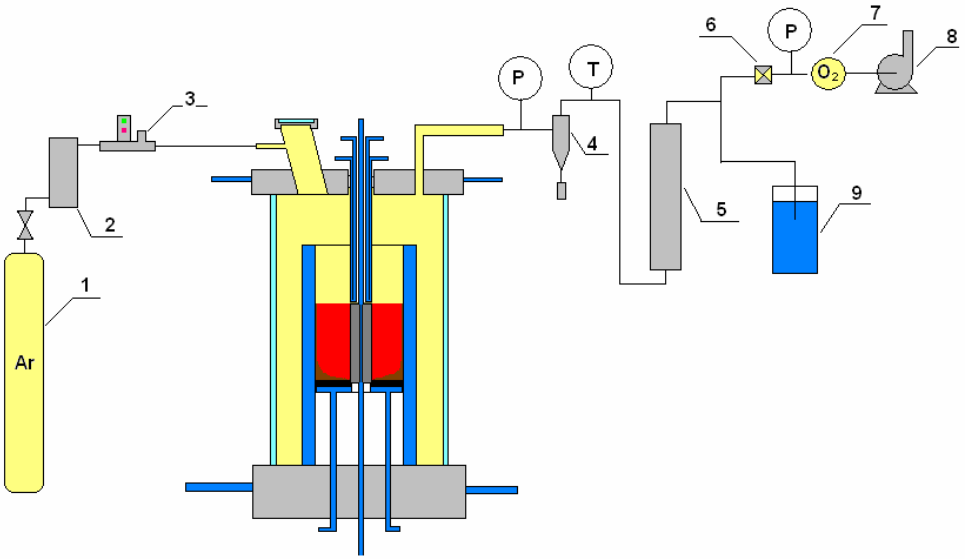

1 – Ar cylinder; 2 – silica gel dehumidifier; 3 – flowmeter; 4 – cyclone; 5 – Petryanov Medium Area Filter (MAF); 6 – Aerosol Analytical Filter (AAF); 7 – electrochemical oxygen sensor; 8 – vacuum pump; 9 – hydraulic lock.

Fig. 1.3 – Gas and aerosols in and out diagram

1.2. Materials

The materials used in the test included 15Kh2NMFA-A vessel steel, urania, zirconia, metallic zirconium and high-purity argon. All oxides and metallic zirconium have been checked for the main substance content. In addition, the powdered urania was checked by thermogravimetry and the oxygen/uranium ratio was found to equal 2.0. The composition of corium charge is given in Tab. 1.2.

Table 1.2

Corium charge composition

Component	Main substance content, %	Impurities, %	Notes
UO_2	>99.0	Fe<0.03; As<0.0003; CuO<0.01; phosphates<0.002; chlorides<0.003.	Certificate data; thermogravimetry
ZrO_2	(ZrO_2+ HfO_2) > 99.4	Al_2O_3 < 0.03; Fe_2O_3 < 0.05; CaO < 0.03; MgO < 0.02; SiO_2 < 0.2; TiO_2 < 0.1; P_2O_5 < 0.15; (Na_2O+K_2O) < 0.02	Certificate data
Zr, Nb-1 alloy	Zr>99.0	Nb < 1.0	XRF

Pr1-MCP-1 pretest has been performed prior to the test. Among its objectives was the preparation of corium C-32. Later on, this corium was milled, thoroughly mixed with urania and zirconia and used as the charge in the main test. Metallic Zr (17.4 g) was used as the start-up material. Composition and masses of the charge components loaded into the crucible are given in Tab. 1.3.

Table 1.3

Charge components composition and masses

Purpose	Component	Fraction, μm	Mass, g	Mass, %
Main charge	Corium from Pr1-MCP-1[1)]	100-200	1400.0	92.5
	Urania, UO_2	<100	86.1	5.7
	Zirconia, ZrO_2	<100	10.2	0.7
	Metallic zirconium, Zr	Wire Ø 5 mm	17.4	1.1
Total			**1513.7**	**100.0**

[1)] – composition determined by XRF and chemical analysis (ChA) is offered in Tab. 2.3

1.3. Experimental procedure

To remove the air fixed in powders and to create an inert atmosphere, the loaded furnace was blasted with argon for approximately 16 min at 10 l/min. At 963 s HF heating was switched on and the molten pool produced. The history of heat fluxes to the cold crucible, specimen and bottom calorimeter during the start-up regime and throughout the test is given in Fig. 1.4, while readings of thermocouples embedded in the vessel steel specimen are shown in Fig. 1.5. By 3550 s the specified temperature of the specimen lateral surface has reached approximately 1400°C. From here on, stability of heat from the melt to the specimen has been maintained for 10 hours by regulating the power in the melt. A thick crust was observed at the pool surface during the test.

At 42000 s from the beginning of the test, HF heating was switched off and the test completed. Melt crystallization to the complete ingot cooling was carried out in argon.

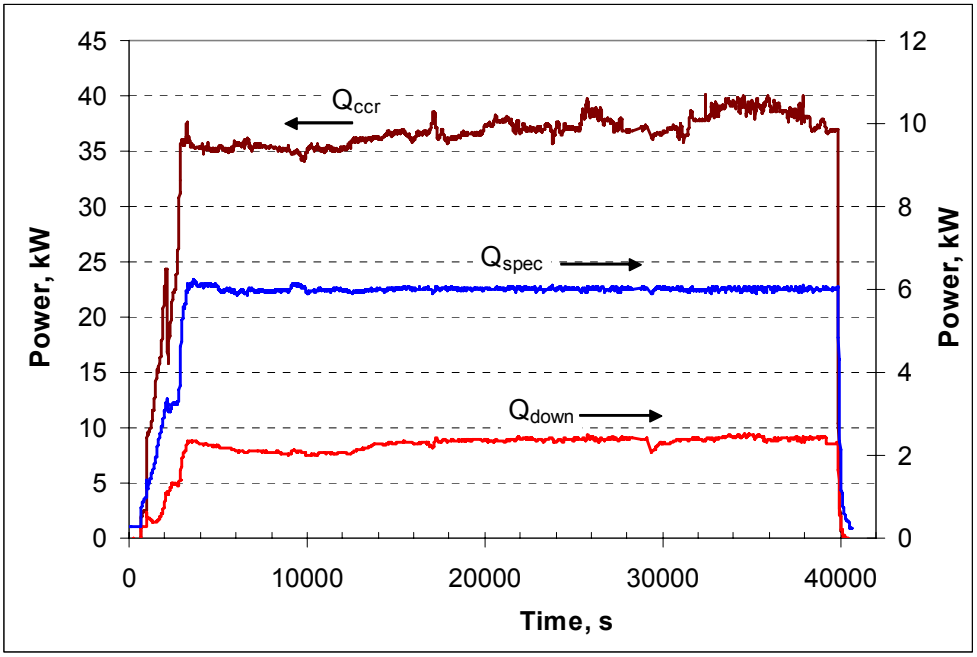

Fig. 1.4 – History of heat fluxes to the cold crucible (Q_{ccr}), specimen (Q_{spec}) and bottom calorimeter (Q_{down})

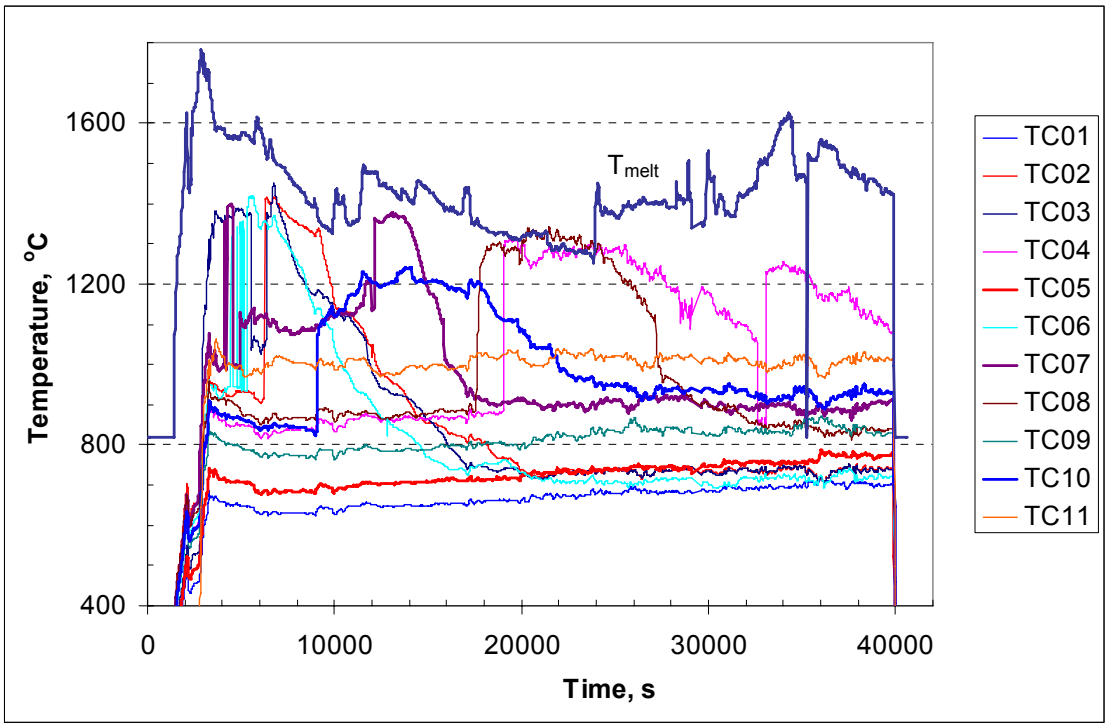

Fig. 1.5 – Thermocouple and pyrometer (T_{melt}) readings in MCP-1

2. POSTTEST ANALYSIS

2.1. Ingot macrostructure

A porous, 38 to 40 mm-thick crust was found above the corium ingot during the furnace disassembly (Figs. 2.1, 2.2). The ingot (Fig. 2.2) was approximately 39 mm high. A ring-shaped metallic body was discovered in the bottom part of the crystallized corium (Fig. 2.3).

The ingot with steel specimen was extracted from the crucible and embedded in epoxy. After epoxy solidification, the block was cut along the axis (Fig. 2.3). One half was used for making a microsection for the SEM/EDX analysis, and the other one – for physicochemical analysis.

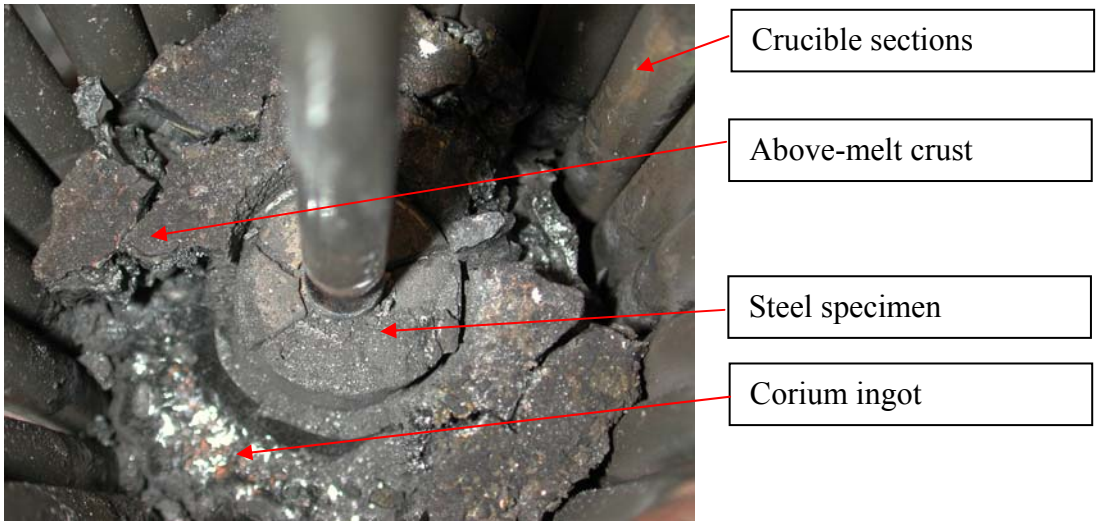

Fig.2.1 – Crucible after the test

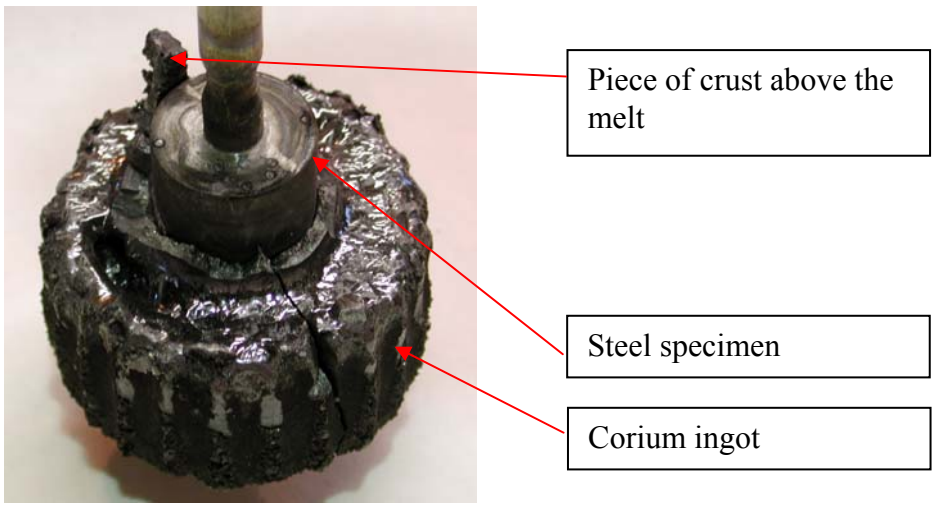

Fig.2.2 – Ingot and steel specimen after extraction from the crucible

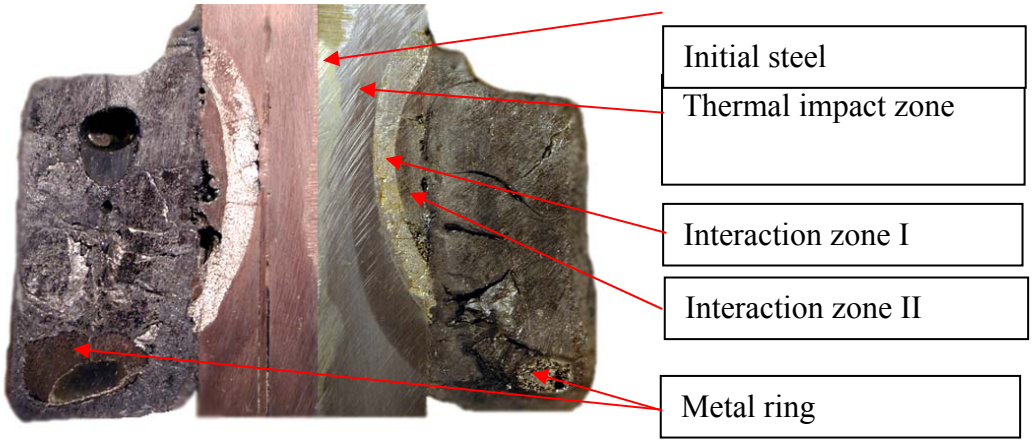

Fig.2.3 – Longitudinal section of steel specimen with corium ingot

2.2. Numeric modeling of the specimen temperature conditions

Interpretation of experimental results requires determination of temperatures at the boundaries of distinctive zones identified in the specimen body during the posttest analysis, as well as of temperature conditions on the specimen surface at the interaction with corium. These parameters can be determined by numerical modeling of the specimen temperature conditions in the axis-symmetrical formulation. A similar procedure has been performed in the posttest analysis for the tests MC6...MC9 [1]. Thermocouple readings were used as the reference temperature values. However, in MCP-1 only one thermocouple was placed in the specimen mid-section where corrosion depth was the biggest. Besides, in contrast to the tests with the specimen location on the bottom and symmetrical profile of heat supply along the top end radius, heat supply conditions in MCP-1 happened to be significantly asymmetrical along the specimen height. Therefore, position of the boundary of phase transition in steel, which had been determined by the posttest analysis and corresponded to 727°C (see Sect. 2.5), was chosen as the reference point when modeling the specimen temperature condition. Besides, the modeling also employed the value of heat power removed from the specimen by the cooling water (N≈6 kW), and – in order to determine boundary conditions of heat removal by the cooling water – the heat exchange/water temperature dependence, in accordance with which the central channel (∅ 3 mm) surface temperature amounted to 110°C.

Boundary conditions for other specimen surface have been set and varied in the following way:

For the specimen upper top, which touched on the water-cooled screen via a ZrO_2 ring-shaped "gasket", heat sink was determined by means of said insulation modeling and setting the temperature on the "gasket" outer side at 20°C.

For the bottom end, the surface temperature was specified to vary linearly from 110°C along the 1.5 mm radius to some varying temperature along the specimen lateral surface radius of 14 mm. The final value of this temperature amounted to 240°C, which is close to 300°C – the temperature measured near the bottom calorimeter (in its midsection) surface, which the specimen "rested" upon when contacting with it along its narrow peripheral surface.

The q=0 thermal insulation condition has been specified for the lower crust zone at 3 mm up from the bottom along the lateral cylindrical surface. The second-order boundary conditions (with different heat fluxes which were varied in variant calculations until the best match with position of the 727°C isotherm) have been specified for the zones of specimen contact with molten corium within the 3 – 45 mm range from the bottom and with the thick corium crust on the rest of the surface (15 mm from the top). The final values of heat fluxes amounted to 0.53 MW/m^2 in the upper part and from 1.71 to 2.05 MW/m^2 in the zone of contact with the melt, increasing upwards linearly in qualitative accord with the oxidic crust that is thinning upwards along the specimen surface (see Sect. 2.4).

To check accuracy of numerical modeling, the results of calculations were compared with thermocouple readings.

It is obvious from Fig. 1.5 that readings of thermocouples embedded in the specimen have a complex nature with sharp (instantaneous on the temporal scale of the test) temperature jumps (200…500ºC). It may be noticed that approximately from 4120 s for some thermocouples values jumped from a relatively low temperature of 850…900ºC up to the level of 1100…1400ºC (thermocouples TC07, 06, 02, 10, etc.). Some time later, the same thermocouples could show a very rapid drop to the previous (or close) level. Such abrupt changes could be demonstrated by one and the same thermocouple several times during the test. It should be noted that hot junctions of all thermocouples with the first recorded jump aimed upward were located in the upper – cold – part of the specimen (see Fig.1.2), while their electrodes were running through hotter areas of the specimen. Apparently, thermoelectrodes short circuited at reaching the channel holding this or that thermocouple by the interaction front. However, points time at jumps of thermocouple readings cannot be directly interpreted as the advance of the interaction front, as there is no certainty in contact between the ∅ 1 mm stainless jacket of a thermocouple and the wall of the ∅ 1.5 mm channel. At the same time, there was a sharp drop from the initial ≈1350ºC down to the level of 1000…1050ºC in readings of thermocouple 03, which hot junction was located at the middle of the specimen height, and it may mean destruction of the very hot junction. Fig. 2.4 presents thermocouple readings selected from Fig. 1.5 and regarded as conventionally reliable. The results of comparison are given in Tab. 2.1. Besides, Fig. 2.5 shows the calculated temperature distribution along the specimen radius 50 mm up off the bottom end, as well as readings of thermocouples located in the same section of the specimen. For some thermocouples which remained operable till the end of the test, the measurements are shown as a temperature range that reflects a slight increase in temperature during the test. For other thermocouples, either initial values, or parts of the range are given. In addition, Fig. 2.5 shows position of the phase transition in the specimen steel at T=727°C. Taking said problems with modeling into account, the results of comparison can be accepted as satisfactory.

Fig.2.6 displays the temperature field in the specimen with plotted phase transition boundaries and two parts of the interaction zone (see Sect. 2.5). Obviously, the maximum deflection of the

phase transition temperature boundary from 727°C is ±10.°C. At the same time, the heat power removed by the cooling water amounted to 5.7 kW, which differs just slightly from the experimentally obtained value. The temperature boundary between the interaction zone and specimen lies within the 1000... 1090°C range. The temperature boundary between two parts of the interaction zone is within the 1240...1300°C range, while the maximum temperature on the specimen surface is 1435°C.

Table 2.1

Experimentally obtained and calculated temperature values in the specimen

Thermocouple No.	R, mm	H, mm	T_{min}, °C	T_{max}, °C	T_{calc}, °C
TC11	12.25	11	1004	1004	952
TC03	12.25	27	1374		1324
TC01	7.25	50	633	700	700
TC09	8.25	50	776	842	750
TC05	9,25	50	687	765	793
TC10	10.25	50	837		830
TC04	11.25	50	838	878	861
TC08	12.25	50	870	909	887
TC02	12.25	50	917		887

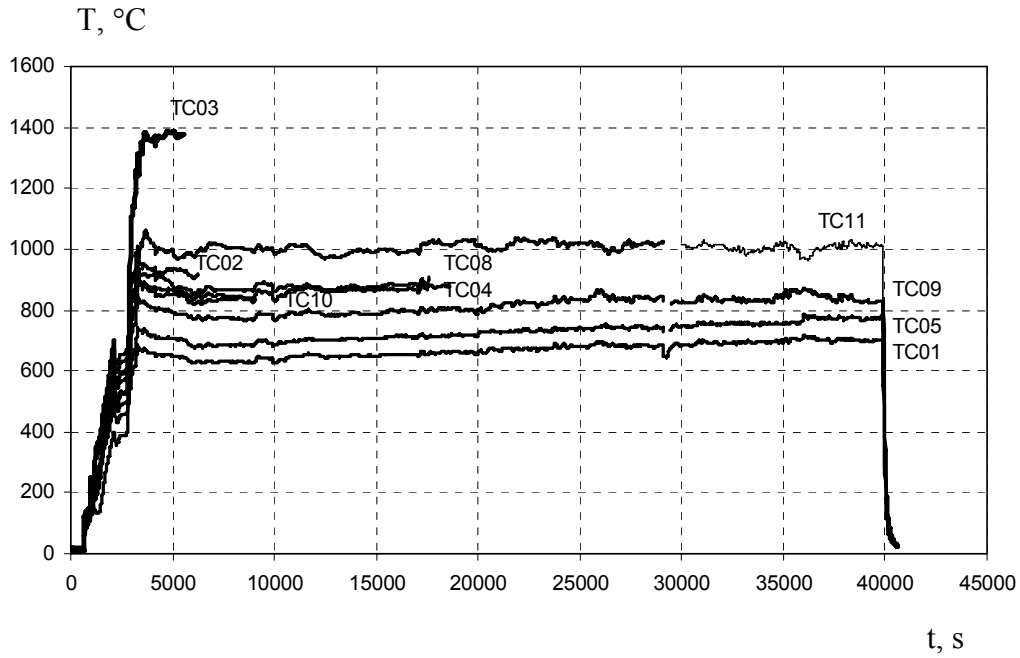

Fig. 2.4 – Reliable thermocouple readings in MCP-1

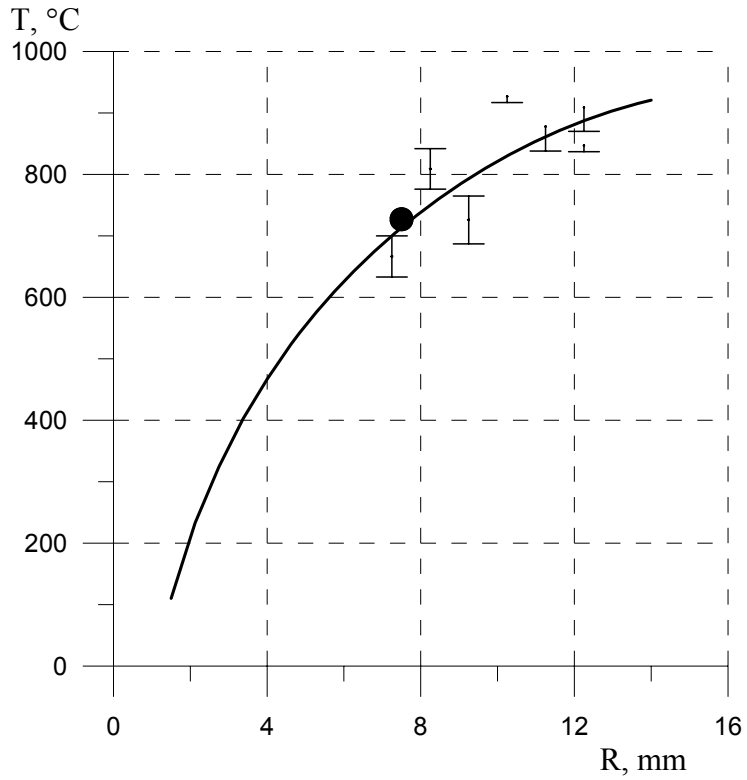

– test; ● – boundary of steel phase transition zone

Fig. 2.5 – Temperature distribution along the specimen radius at 50 mm above the bottom end

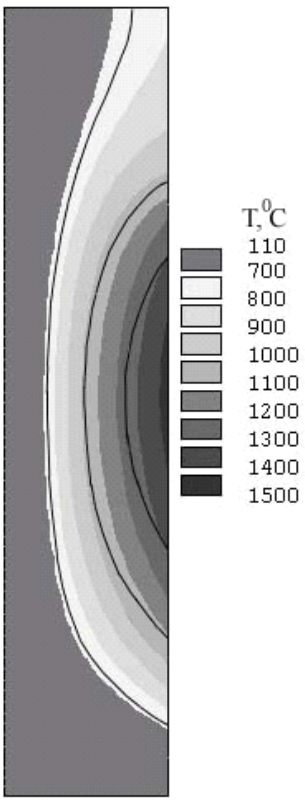

Fig. 2.6 – Temperature field in the specimen

2.3. Physicochemical analysis

2.3.1. Mass balance of the test

In order to make the mass balance, the initial charge components and fused products were weighed with a 0.1 g accuracy and then analyzed for the content of main components.

Mass balance for MCP-1 is given in Tab. 2.2.

Table 2.2

MCP-1 mass balance

Introduced into the melt, g		Collected after the test, g	
Corium from Pr1-MCP-1[3)]	1400.0	**Above-melt crust**	486.9
UO_2	86.1	**Ingot[1)]**	976.6+steel
ZrO_2	10.2	**Spillages[2)]**	49.3
Metallic Zr	17.4	**Aerosols**	0.9
Σ	**1513.7**	**Σ**	**1513.7+steel**

[1)] – The mass of the ingot is given as the total mass of the introduced components minus summarized mass of products which did not participate in melting.
[2)] – The spillages include charge material (urania and zirconia mixture in a ratio specified at loading).
[3)] – Physicochemical data on the ingot composition from Pr1-MCP-1 is offered in Tab. 2.3.

It was impossible to determine the exact mass of the corium ingot, as after the test it was embedded in epoxy together with the steel specimen. Tab. 2.2 gives its mass as the total mass of the introduced components minus summarized mass of products which did not participate in melting. The mass of steel components which transited from the steel specimen into molten corium during the test was added to the mass of ingot. Due to the reason given above, Tab. 2.2 does not contain debalance of the test.

It was mentioned earlier that corium C-32 fused in Pr1-MCP-1 pretest and then crushed down into 100-200 μm-sized particles was used as the main charge material. An average sample obtained by quartering was further ground into particles below 50 μm and subjected to XRF and ChA. Preparation of samples for analyses was carried out in argon. The results of physicochemical analysis of the corium average sample from Pr1-MCP-1 are offered in Tab. 2.3.

Table 2.3

Physicochemical analysis of an ingot average sample from Pr1-MCP-1

Test	Detection method			
	XRF		Chemical analysis	
	Composition, mass %			
Pr1-MCP-1	**U**	67.6	**U**	68.0
	Zr	21.5	**Zr**	21.5
	Impurities and O[1)]	10.9	**Impurities and O[1)]**	10.5

[1)] – impurities and oxygen determined from residue

The volumetric method [2, 3] was applied to determine free zirconium in the average sample which was found to be 15.1 mass % and correspond to corium C-29.8.

2.3.2. XRF of the witness specimen and fused products

The elemental composition of the witness specimen and fused products was determined by XRF using the SPECTROSCAN MAX-GV vacuum spectrometer. The vessel steel witness specimen represented a disk ∅ ~15 mm lathed from the cylindrical specimen blank.

Tab. 2.4 contains the XRF results for the vessel steel witness specimen compared with Specifications for the vessel steel of this grade.

Table 2.4

XRF data on the vessel steel witness specimen composition

TU, analytical method	Chemical elements content, % mass												
	Al	C	Si	Mn	Cr	Ni	Mo	V	P	S	Cu	Co	As
TU 108-765-78		0.13-0.18	0.17-0.37	0.30-0.60	1.8-2.3	1.0-1.5	0.5-0.7	0.10-0.12	<0.02	<0.02	<0.3	<0.03	<0.003
XRF	0.356	-	0.193	0.440	2.08	1.14	0.518	0.096	-	-	0.234	-	0.002

XRF has confirmed correspondence of 15Kh2NMFA-A steel used in the test to TU 108-765-78.

Upon completion of MCP-1, one half of the corium ingot with steel specimen was cleaned of epoxy and the corium ingot conventionally divided into two parts: ingot top (h=16 mm, m=182.4 g) and ingot bottom (h=23 mm, m=281.6 g). Explanations to Tab. 2.2 mention that the exact mass of corium ingot could not be determined after the test, though masses of the ingot halves made it possible to approximately assess the total ingot mass at 928.0 g. Masses of these ingot parts were further used for composing the elemental material balance.

Average samples for XRF and chemical analysis have been produced from the upper and bottom parts of the ingot and above-melt crust by quartering and further grinding into particles no more than 50 μm. The bottom part was crushed together with the ring-shaped metallic body (see Sect. 2.1).

A sample for XRF representing a flat plate ~10×5 mm^2 was cut from the interaction zone (Fig. 2.7), polished and analyzed from both sides (i.e., from the steel specimen and corium sides). The plate was cut in such a way that it covered both interaction zone I (see Fig. 2.3) and zone II (see Fig. 2.3), which is conventionally marked as zone III in Fig.2.7. A similar sample was cut from the ring-shaped metallic body (see zone V in Fig. 2.7). The sample from zone IV, representing a ~100 mg particle, has been subjected to chemical analysis.

Preparation of samples for analyses was done entirely in argon. Fig. 2.7 shows the zones from which samples were taken for posttest analyses: **x –** chemical analysis (zone IV); **O** – XRF (zones III, V).

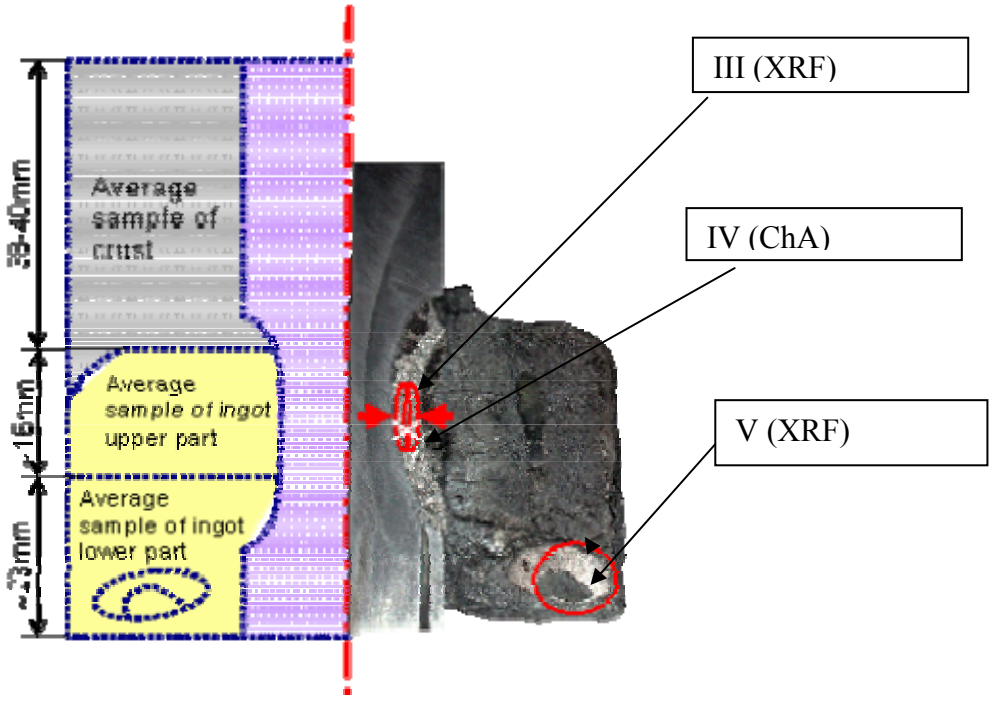

Fig. 2.7 – Ingot macrostructure and pattern of taking samples for XRF and chemical analysis

Tab. 2.5 contains the XRF results for samples from MCP-1.

Table 2.5

XRF results for samples from MCP-1

Sample	Content, mass %					Note
	U	Zr	Fe	Cr	Ni	
Above-melt crust	66.5	20.2	1.69	0.06	0.02	Regression analysis, fundamental parameters method (FPM)
Ingot top	66.1	22.3	1.0	0.02	0.03	Regression analysis
Ingot bottom	64.6	21.7	3.5	0.04	0.08	Regression analysis
Zone III-II from the corium side	51.7	13.5	30.9	0.6	0.3	FPM
Zone III-I from the specimen side	36.5	14.3	47.8	0.8	0.5	FPM
Zone V	57.5	24.2	17.8	0.21	0.27	FPM

The regression analysis is a quantitative XRF analysis that employs SPEKTR-KVANT software. Its essence is in applying the multiple regression method for calculating concentrations of elements from the measured intensities of their characteristic X-ray lines taking into account the calculated (during calibration of the X-ray spectrometer) calibration equation coefficients. This kind of analysis requires taking into account instrumental drift by referring to measurements of the reference specimen, and also of the background in different ways (using points, incoherent scattering lines, blank sample).

When the regression analysis was applied, the error in U, Zr and Fe content determination by XRF did not exceed 5 relative %.

FPM is a method of qualitative and quantitative X-ray fluorescence analysis in the absence of reference specimens. The method is based on the use of theoretical dependences that describe physical processes of X-ray fluorescence excitation in a sample and subsequent registration of this radiation by spectrometer. The numerical code employing the method is adjusted on a particular spectrometer using the high-quality calibration specimens which cover the entire range of instrument operation (all crystals and wavelengths). FPM allows calculation of concentrations of virtually any set of the determinable elements in the studied sample without the use of calibration specimens. Relative errors of the quantitative reference-free analysis depend on content of the determined elements and amount to:

- about 2 relative % in the 0.1 – 1.0 mass.% range,
- 3 – 5 relative % in the 1.0 – 5.0 mass.% range,
- 1 – 3 relative % in the 5 – 10 mass.% range,
- 0.5–2 relative % in the range over 30 mass.%.

With reference samples, accuracy of the quantitative analysis by FPM is compared well with that of the regressions analysis.

As for the nonidentifiable elements (e.g., oxygen), their content should be determined by other methods (e.g., by carbothermal reduction), or there should only be known ratio of their content (light matrix composition), e.g., the chemical formula (H_3BO_3, HCl, etc.).

The use of the fused products XRF data renormalized to account for oxygen measured by the carbothermal reduction method (CTR) (see Tab. 2.19 Sect. 2.6) made it possible to compose the elemental mass balance (see Tab. 2.6).

Renormalizing employed average values of oxygen content obtained by CTR.

The below assumptions were accepted when making the elemental material balance:

– 0.9 g of aerosols were collected during the test and not analyzed because of small quantity. Since the test was performed in an inert atmosphere and throughout the test there was a crust above the melt, aerosols were supposed to be mainly composed of UO_2;
– spillages were not analyzed, too, therefore Tab. 2.6 gives their composition proceeding from the powdered materials (UO_2/ZrO_2) ratio in the initial charge (see Tab. 2.2);
– masses of the interaction zones I and II (Fig. 2.3) were obtained by calculations based on the calculated volumes of these zones. Zone I volume was 6436 mm^3 (V_1), while that of zone II (V_2) – 4364 mm^3 (see Fig. 2.8). Densities of these zones were determined in accordance with their compositions by additive calculations and amounted to 11.55 g/cm^3 and 13.56 g/cm^3, respectively.

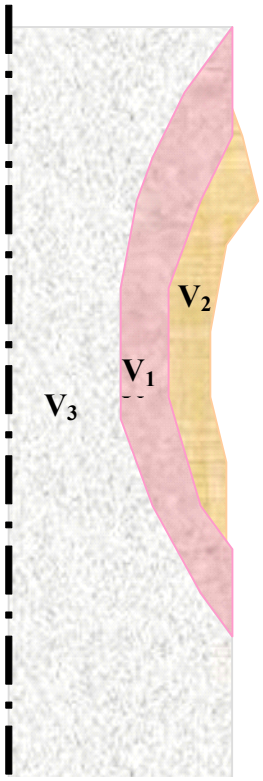

V_1- volume of interaction zone I; V_2- volume of interaction zone II; V_3- volume of the non-corroded steel specimen.

Fig. 2.8 – Steel specimen and interaction zones (IZ) diagram

Table 2.6

XRF data on the fused products (taking CTR into account) and elemental mass balance for MCP-1

Sample	U	Zr	Fe(Cr, Ni)	O	Mass, g	U	Zr	Fe(Cr, Ni)	O
	mass %					g			
Above-melt crust	66.1	20.1	1.8	12.1	486.9	321.6	97.7	8.6	59.0
Ingot top	65.6	22.1	1.0	11.3	364.8	239.2	80.7	3.8	41.2
Ingot bottom	64.4	21.7	3.5	10.4	563.2	362.7	122.4	19.7	58.5
Zone III-II (from the corium side)	52.4	13.7	32.2	1.7	59.2	31.0	8.1	19.1	1.0
Zone III-I (from the specimen side)	36.4	14.3	49.1	0.2	74.4	27.1	10.6	36.5	0.2
Spillages	68.3	20.6	-	11.1	49.3	33.7	10.2	-	5.5
Aerosols	88.1	-	-	11.9	0.9	0.8	-	-	0.1
Collected in the end of the test					-	1016.1	329.7	87.6	165.4
Introduced into the melt					-	1022.3	326.0	0.0	165.5
Δ					-	-6.2	+3.7	+87.6	-0.1

The amount of steel that transited into molten corium was calculated to be ~85 g. This value is based on the facts that the initial volume of steel before interaction was ~35813 mm^3, the volume of the non-corroded steel was 25013 mm^3 (V_3), and density of steel is ~7.87 g/cm^3. A slight discrepancy between the calculated mass of Fe(Cr, Ni, Mn) – 85 g and that obtained by XRF – 87.6 g (see Tab. 2.6) is apparently due to the error in volumes determination, or to nonuniformity of the IZ composition.

It follows from the data presented in Tab. 2.6 that the degree of corium oxidation reduced during the test from C-30 to C-17. Apparently, this is due to free zirconium repartitioning between molten corium and solid crust (see Tab. 2.7), which was located above the melt surface and did not participate in the interaction with the steel specimen. The data from Tab. 2.6 also helped to determine that the mass of steel fraction that participated in the interaction amounted to 7.1 mass % of the total mass of the interaction zone and molten corium.

2.3.3. Chemical analysis of the fused products

The pattern of samples selection for analyses is shown Fig. 2.7.

Preparation of samples for analyses employed the technique of fusing 0.1…0.5 g samples from the ingot and other fused products with 3.0±0.5 g of potassium pyrosulphate at 900±25ºC until the appearance of a transparent alloy, which was further dissolved at heating it in 200…250 ml 1M solution of sulphuric acid. Then the total zirconium was determined as Zr^{4+} by photometry with orange xylenol, U with arsenazo III, and Fe with orthophenanthroline. Free zirconium Zr_{free} was determined by volumometry.

The method of total Zr determination is based on the formation of a colored complex compound of Zr (IV) and orange xylenol in the sulphuric acid solution with molar concentration of the equivalent of 0.3 – 0.4 $mole/dm^3$ [4-6]. The evaluation of zirconium is not complicated by large quantities of Mo, W, U, Zn and Ti, as well as impurities of Fe (up to 50 μg), Pb, Ni, Cu, Th and Ta (>100 μg) [3,4].

The technique of U determination with arsenazo III is meant for the determination of uranium microquantities in samples without uranium separation, with a sensitivity of 0.04 μg/ml [7, 8].

The content of Fe was determined by photocolorimetry with orthophenanthroline. The method is meant for the determination of iron oxides content in samples of the uranium-bearing corium without uranium separation [9]. The range of identified iron concentrations is 0.4-400 mg/dm^3. The total relative error of the method does not exceed ±3%, provided the measured optical densities are within 0.2-0.6 range. The method is based on the reaction of orthophenanthroline with ferrous iron ions at pH around 3-9, which yields a complex compound with an orange-red colouring, which develops rapidly at pH=3.0-3.5 in presence of excessive orthophenanthroline and keeps stable within several days. The mass concentration of total iron is determined by reducing ferric iron to ferrous iron by hydroxylamine in acid medium, and then ferrous iron is determined directly. The amount of ferric iron is calculated from the difference between the content of ferrous and total iron [10,11].

Free zirconium was determined applying the technique [2, 3] by volumometry, which is based on the dissolution of free zirconium in phosphoric acid that yields 2 moles of hydrogen per each gram-atom of zirconium.

The results of the fused products chemical analysis are given in Tab. 2.7.

Table 2.7

Chemical analysis of the fused products

Sample	Content, mass %			
	U	Zr	Zr_{free}	Fe
Above-melt crust	66.8	22.3	12.0	2.1
Ingot top	66.6	23.2	14.0	1.0
Ingot bottom	66.7	22.3	15.2	5.7
Zone IV	54.6	15.9	n/determ.	28.5

The error of U content determination by photocolorimetry did not exceed 5 relative %, and that of Zr and Fe determination was not above 3 relative %.

A comparison of the XRF (Tabs. 2.5, 2.6) and chemical analysis (Tab. 2.7) results concerning the main components in the fused products has shown them to be in satisfactory accord.

Physicochemical analysis (XRF and chemical analyses) have shown that a part of steel components transit into molten corium at the interaction between corium and steel specimen (see Tabs. 2.5, 2.6), and the interaction zone and "metallic' ring on the oxidic ingot bottom are composed of uranium, zirconium and components of steel with a small quantity of oxygen (see Sect. 2.6).

2.4. SEM/EDX analysis of corium and steel

A polished section for SEM/EDX was produced from a half of the steel specimen longitudinal section (Fig. 2.9). Visual examination of the polished section makes it possible to speak about at least two-layer structure of the degraded steel specimen, of the two-layer structure of the crystallized corium, and of metal-rich inclusions in the crystallized corium. SEM/EDX was used to investigate the steel/corium interaction zone (Fig. 2.9, zones 1, 3-8), the crystallized corium away from the interaction zone (Fig. 2.9, zones 1 and 2), and the metal-rich inclusion in the crystallized corium (Fig. 2.9, zones 9-12).

EDX results for steel from different parts of the polished section (Tab. 2.8, point P8 and points 1-6) did not differ much and showed correspondence to mol. % 94.3 Fe, 2.5 Cr, 1.3 Ni, 0.5 Mn, 1.0 Si, 0.3 Mo.

Let's consider structure of the interaction zone in the direction from steel to crystallized corium. Fig. 2.10 presents a composed of micrographs image of zone I, which is located where the interaction front had penetrated steel the deepest and which stretches along the entire interaction zone up to the shrinking pore in the crystallized corium. The interaction zone/steel boundary is smooth, it being the evidence that the system had attained stationary conditions. Microstructurally, the layer adjacent to steel is uniform along the entire height of the zone, except for the very top part (Fig. 2.9, region 3). Structure of the zone in the direction from steel to crystallized corium is nonuniform. At least four layers can be distinguished:
- a light-coloured layer adjacent to the steel specimen, impregnated by faceted crystallites,
- a dark, uniform, highly porous layer, in some places cut by heavy component-rich veins all the way through,
- a layer with the dendritic, heavy component-rich crystallized microstructure,
- a uniform layer separating the interaction zone from the crystallized corium.

The diffuse penetration of U (and of Zr with it) into the steel specimen, which is very typical of the tests in the MC series, is observed at the boundary of interaction with steel (Fig. 2.11, region 1-1, Tab. 2.8, points P5-P7, Fig. 2.15, region 3-1, Fig. 2.18, region 7-1).

The layer adjacent to steel (Fig. 2.11, region 1-1-1-1, Fig. 2.15, region 3-1, Fig. 2.17, regions 5 and 6, Fig. 2.18, regions 7-1 and 7-2) shows at least two phases long the entire polished section, that is, a phase based on the intermetallic compound $U(Zr)Fe_{2.5}(O)$ (Fig. 2.11, Tab. 2.8, points P1, P3, Fig. 2.15, Tab. 2.12, points P1, P3, Fig. 2.18, point P1) and crystallized as a "labyrinth" structure, except for zone 3 (Fig. 2.15, region 3-2), in which it had crystallized as satellite grains of the 2nd phase based on the intermetallic compound $Zr(U)Fe_{3.5}(O)$ (Fig. 2.11, Tab. 2.8, point P2, Fig. 2.15, Tab. 2.12, point P2, Fig. 2.18, point P2) found in the form of faceted crystallites along the entire boundary. The central and lower areas of zone 3 also showed the presence of an intermediate microstructure in quantities insufficient for identification by EDX. Micrograph of region 3-2-1 presents it as a two-phase crystallized eutectic composition (Fig. 2.15, region 3-2-1, Tab. 2.12, square SQ1, point P5). Region 3-3 is a transitional one, from that predominantly composed of the $(U,Zr)Fe_{2.5}(O)$ intermetallide, to the practically monophase region, with the eutectic composition crystallized in between.

The monophase layer – the widest in the interaction zone – is represented by an intermetallic phase with a composition constantly changing from $U(Zr)Fe_{2.5}(O)$ (Fig. 2.11, region 1-1-2, Tab. 2.8, point P9 and square SQ3) to $Zr(U)Fe_2$ (Fig. 2.12, regions 1-2-1 and 1-2-2, Tab. 2.10, points P1, P5, square SQ1).

The nature of the arterial channels observed in the considered zones and filled with the phase based on the $U(Zr)_{1.5}Fe$ intermetallic compound, is most likely due to the filling of the arterial channels, a system of which form at cooling, with a fusible phase (Fig. 2.17, Tab. 2.14, points P1 и P2).

The monophase layer is followed by another one with the dendritic crystallized microstructure (Fig. 2.12, region 1-2), which evidences that this layer stayed liquid during the test right until crystallization of the system upon cutting power to the melt off. In this region, a refractory phase based on the $U(Zr)O_2$ solid solution $U(Zr)O_2$ (Fig. 2.12, Tab. 2.9, points P3 and P8) co-crystallizes with the $Zr(U)Fe_2$–based one (Fig. 2.12, region 1-2-2, Tab. 2.9, points P6 and P9; Fig. 2.16, region 4-4-1, points P6 and P7). A eutectic mixture of two phases has crystallized in between the considered phases. The eutectic composition is given in Tab. 2.13 (SQ5) and is in accord with the known phase diagram of the U-Fe system. The phases composing the eutectic structure are also presented in Tab. 2.13 ($U(Zr)_6Fe$ – P4 and $U(Zr)Fe_2$ – P5). Towards the crystallized corium, the amount of the $U(Zr)O_2$-based refractory oxidic phase keeps increasing in the zone concerned.

The next layer past the considered zone is composed of a practically monophase solid solution based on $U(Zr)O_2$ (Fig. 2.12, regions 1-2-4 and 1-2-5, points P11, Fig. 2.13, region 1-3-1, square SQ1). This layer grows thicker towards the lower edge of the polished section (Fig. 2.9) and is less than 1 mm in the upper part of the interaction zone (Fig. 2.16, regions 4-2 and 4-3).

The next layer has a microstructure typical of the incompletely oxidized corium: it is composed mainly of two phases, that is, a phase based on the $U(Zr)O_2$ solid solution (Fig. 2.13, point P1) and an α-Zr(O)-based phase (Fig. 2.13, point P2). The crystallized corium is uniform in terms of microstructure and composition in all the investigated zones (Fig. 2.13, region 1-3-3, square SQ2, Fig. 2.14, regions 1-4, 1-5-1, 2, squares SQ1, SQ2).

At the same time, inclusions with a microstructure characteristic of the metallic part of the melt from the MA series of MASCA project have been observed in the lower part of the polished section and near the shrinking cavity. The metallic body located at the bottom was entire and completely encircled the steel specimen (Fig. 2.19). Bulk composition of the zone concerned is presented in Tab. 2.16 (squares SQ1 and SQ2). The finely dispersed and multiphase character of

crystallization prevents exact registration of all the coexisting phases, still it is possible to identify intermetallides based on $(Zr,U)Fe_2$, $Zr(U)_2Fe$, $Zr(U)_3Fe$, U_6Fe (Tabs. 2.16 and 2.17). Besides, there should be mentioned the isolation of oxidic globules in the metallic component and metallic globules in the oxidic component. This was characteristic of the tests in the MA series and demonstrated the effect of the secondary stratification during crystallization of immiscible liquid phases (Fig. 2.19, regions 9-1, 9-2-1, 10, Tab. 2.16, point P7; Fig. 2.20, region 12-1). Therefore, it can be stated that stratification of the liquid phase and the effect of secondary isolation of liquids during melt crystallization have occurred in the present test.

The absence of vast areas of eutectic crystallization observed in the tests with horizontal positioning of the steel specimen, as well as the presence of wide monophase layers in the interaction zone evidence in favour of a somewhat different mechanism of the interaction zone formation in the test with vertical positioning of the steel specimen. For instance, the liquid phase that forms at the boundary with steel, being probably less dense than the solid phases that form in the interaction zone, is forced out into the upper part of the zone. As a result, phases in equilibrium with the corresponding temperature zones, grow in the interaction zone. When the isotherm equal to the melting temperature of the $Zr(U)Fe_2$ mixed (the Laves phase) intermetallide is reached, there occurs melting and accumulation of a liquid phase, the transition of which into the melt is blocked by a layer of the $(U(Zr)O_2)$ refractory phase, it being the phase of primary crystallization on the cooled specimen from the melt during pool formation. This layer is the thinnest in the upper part of the zone, and probably it makes it possible for the liquid phase that had accumulated in the interaction zone, to escape into the melt (Fig. 2.16, regions 4, 4-2, 4-3).

When assessing kinetics of the interaction process on the vertical wall, it is equally possible to suppose acceleration of the interaction front advance (compared to the interaction on the horizontal surface) at the expense of the constant supply of the interaction zone with reagents due to the permanent transition of components into the melt, and retardation of the process because there forms a barrier of the monophase layer. In any case, the boundary temperature of the interaction front, which is determined by the liquid phase composition right near the steel specimen, should not differ significantly from the boundary temperature recorded in the tests with horizontal positioning of the steel specimen, with other conditions being equal. Also, it should be mentioned that formation of the lamellar structure of the interaction zone is connected with the equilibrium phase change under specific temperature conditions. If relevant data on the limits of this or that compound existence were available, it would have been possible to compare them with the calculated temperature field distribution in the interaction zone.

The liquid-phase stratification in the melt and the presence of a big amount of steel components in the crystallized metal-rich component also confirm the supposed escape of the liquid into the melt from the interaction zone.

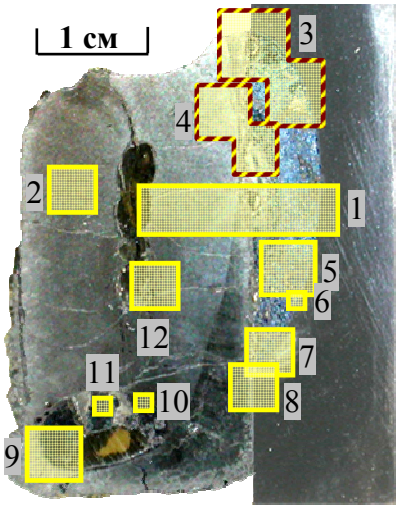

Fig. 2.9 – Polished section from MCP-1 with regions marked for SEM/EDX examination

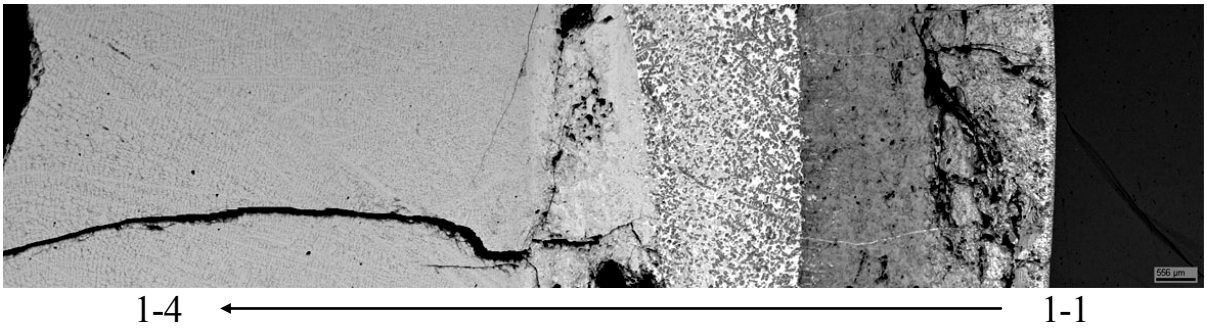

Fig. 2.10 – Micrographs of region 1

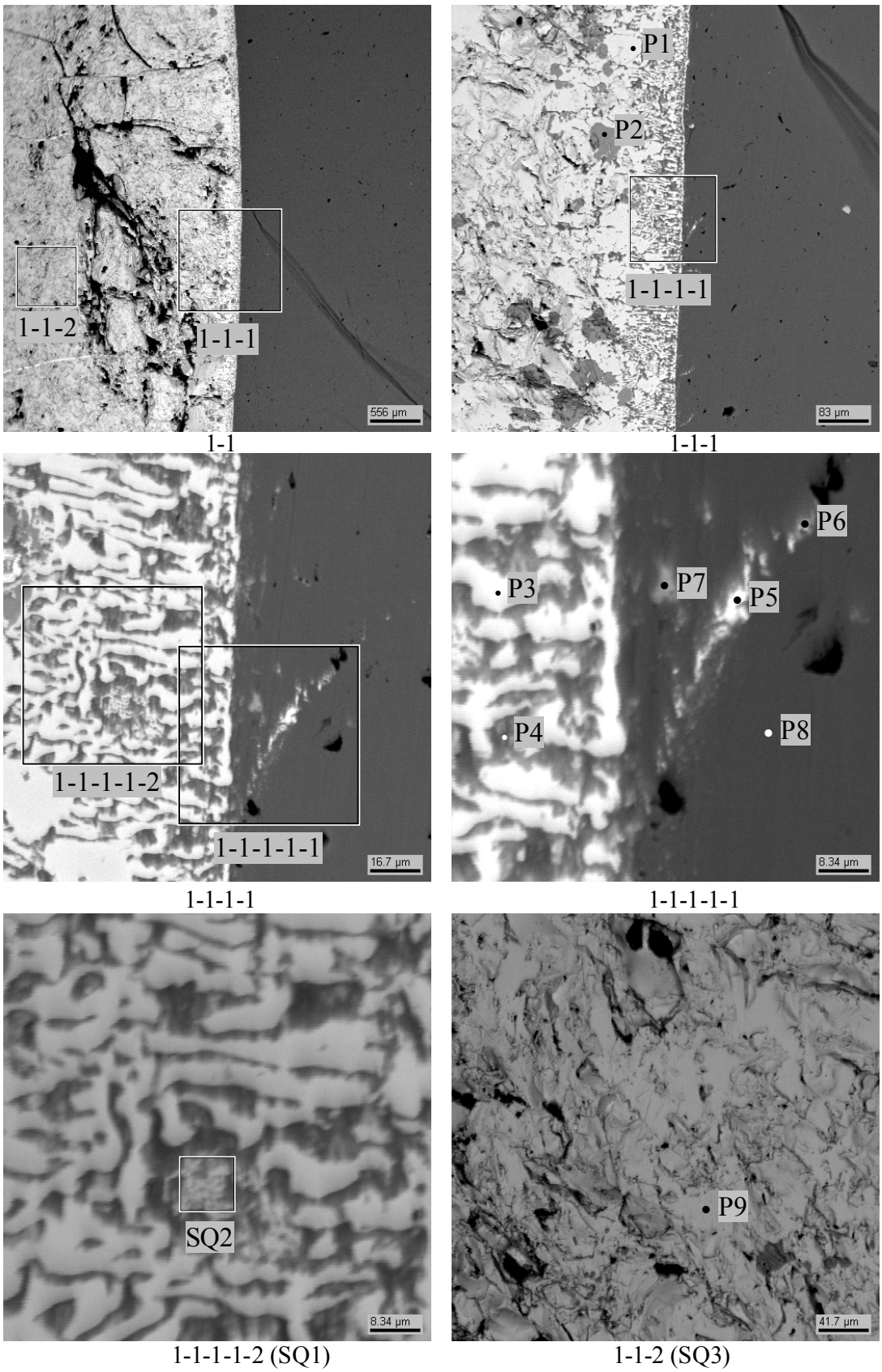

Fig. 2.11 – Micrographs of region 1-1

Table 2.8

EDX data for region 1-1

No.		U	Zr	Fe	Cr	Ni	Si	Mn	Mo	~O	Phase
SQ1	mass %	38.29	6.92	51.19	1.85	0.84	0.30	0.28	0.32	-	-
	mol. %	13.16	6.20	74.98	2.90	1.17	0.89	0.42	0.27		
SQ2	mass %	32.46	25.38	39.64	1.60	0.49	0.21	0.23	-		-
	mol. %	11.61	23.68	60.41	2.62	0.71	0.62	0.36			
SQ3	mass %	47.25	8.04	35.57	1.06	0.64	0.77	-		6.66	$U(Zr)Fe_{2.5}$
	mol. %	14.19	6.30	45.53	1.46	0.79	1.97			29.76	
	mol. % MeO_x	20.20	8.97	64.82	2.08	1.12	2.81				
P1	mass %	55.11	5.12	37.98	0.50	0.63	0.44	0.22	-		$U(Zr)Fe_{2.5}$
	mol. %	22.98	5.57	67.50	0.95	1.06	1.54	0.40			
P2	mass %	15.04	22.41	59.31	1.28	0.61	1.07	0.28	-		$Zr(U)Fe_{3.5}$
	mol. %	4.36	16.95	73.29	1.71	0.71	2.62	0.35			
P3	mass %	60.35	-	37.74	1.14	0.40	0.15	0.22	-		UFe_3
	mol. %	26.21		69.86	2.26	0.70	0.56	0.41			
P4	mass %	57.24	6.27	35.09	0.55	0.60	0.25	-			$U(Zr)Fe_2$
	mol. %	24.86	7.11	64.97	1.09	1.05	0.92				
P5	mass %	22.49	7.34	65.80	2.53	0.75	0.30	0.36	0.43	-	matrix capture (steel)
	mol. %	6.58	5.60	82.03	3.39	0.89	0.75	0.46	0.31		
P6	mass %	7.99	-	86.77	2.60	1.16	0.40	0.45	0.63	-	
	mol. %	1.99		92.15	2.96	1.17	0.84	0.49	0.39		
P7	mass %	11.63	41.41	44.02	2.17	0.31	0.18	0.29	-		
	mol. %	3.62	33.63	58.40	3.09	0.39	0.48	0.39			
P8	mass %	-		94.44	2.44	1.32	0.48	0.60	0.72	-	steel
	mol. %			94.16	2.61	1.26	0.95	0.61	0.42		
P9	mass %	53.46	6.11	38.62	0.74	0.54	0.23	0.31	-		$U(Zr)Fe_{2.5}$
	mol. %	22.01	6.56	67.77	1.40	0.89	0.81	0.55			

Statistics of EDX data for steel

No.		Fe	Cr	Ni	Si	Mn	Mo
1	mass %	94.57	2.43	1.44	0.50	0.46	0.60
	mol. %	94.23	2.60	1.36	0.99	0.47	0.35
2	mass %	94.83	2.23	1.29	0.73	0.36	0.56
	mol. %	94.27	2.39	1.22	1.45	0.36	0.32
3	mass %	94.80	2.27	1.46	0.48	0.40	0.59
	mol. %	94.48	2.43	1.38	0.95	0.41	0.34
4	mass %	94.19	2.46	1.53	0.54	0.56	0.73
	mol. %	93.87	2.63	1.45	1.06	0.56	0.42
5	mass %	94.92	2.25	1.36	0.36	0.56	0.56
	mol. %	94.69	2.41	1.29	0.72	0.56	0.32
6	mass %	94.76	2.35	1.42	0.61	0.43	0.43
	mol. %	94.25	2.51	1.35	1.21	0.43	0.25

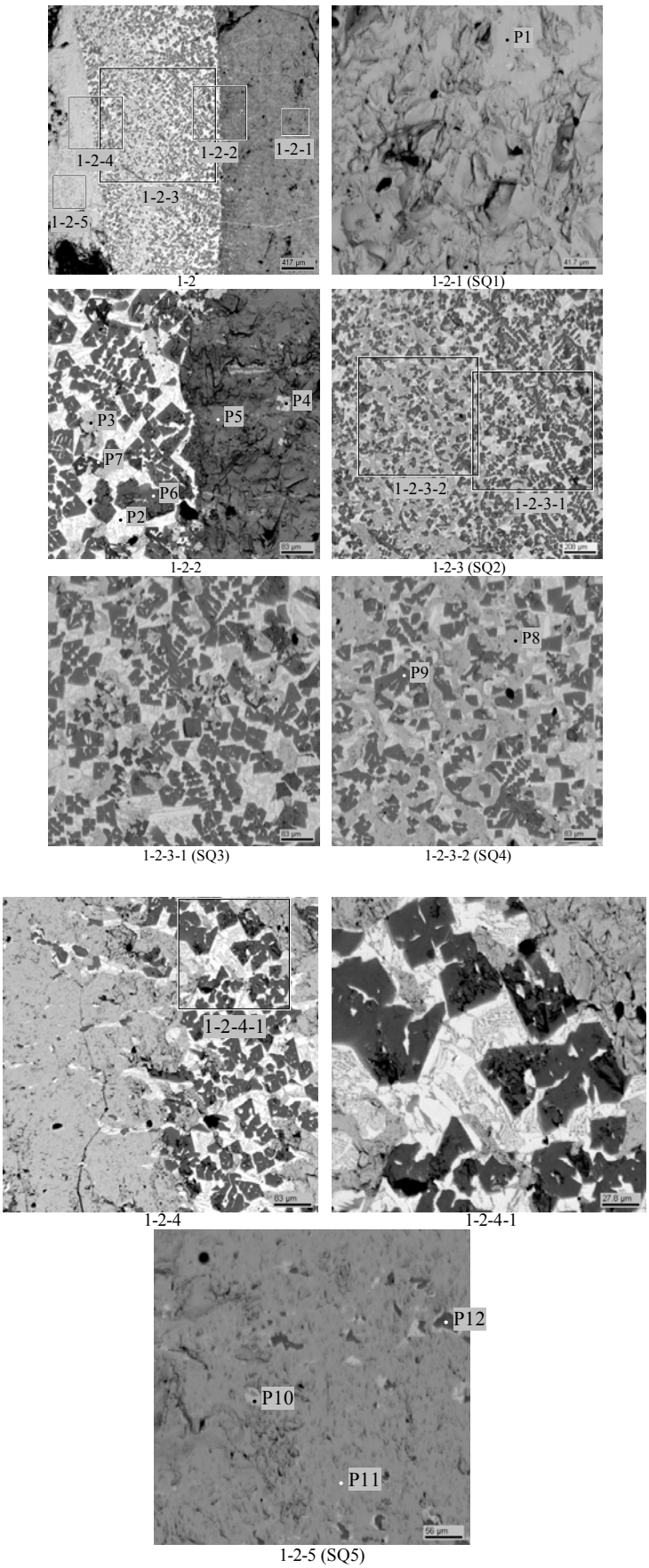

Fig. 2.12 – Micrographs of region 1-2

Table 2.9

EDX data for region 1-2

No.		U	Zr	Fe	Cr	Ni	Si	Mn	Mo	~O	Phase
SQ1	mass %	32.81	11.08	41.60	1.31	0.67	0.78	-	0.37	11.38	$(U,Zr)Fe_3$
	mol. %	7.73	6.81	41.76	1.41	0.64	1.55		0.22	39.88	
	mol. % MeO_x	12.85	11.33	69.46	2.35	1.06	2.58		0.36		
SQ2	mass %	60.89	14.66	21.48	0.82	0.43	0.32	-		1.40	-
	mol. %	27.71	17.41	41.66	1.70	0.80	1.25			9.48	
	mol. % MeO_x	30.61	19.23	46.02	1.88	0.88	1.38				
SQ3	mass %	56.41	18.24	22.96	0.71	0.48	0.29	-		0.90	-
	mol. %	25.30	21.35	43.90	1.46	0.87	1.11			6.02	
	mol. % MeO_x	26.92	22.72	46.71	1.55	0.92	1.18				
SQ4	mass %	66.41	12.07	18.54	0.62	0.30	0.18	-		1.89	-
	mol. %	31.54	14.95	37.52	1.35	0.57	0.72			13.35	
	mol. % MeO_x	36.40	17.26	43.30	1.55	0.66	0.83				
SQ5	mass %	77.34	3.52	1.80	-		0.18	-		17.16	$U(Zr)O_2$
	mol. %	22.03	2.61	2.18			0.45			72.73	
	mol. % MeO_x	80.78	9.58	8.00			1.63				
P1	mass %	39.49	14.88	43.28	1.09	0.60	0.36	0.29	-		$(U,Zr)Fe_{2.5}$
	mol. %	14.38	14.15	67.19	1.82	0.89	1.12	0.46			
P2	mass %	92.69	1.70	5.25	-	0.36	-				$U(Zr)_4Fe$ two phases mixed
	mol. %	76.63	3.66	18.51		1.21					
P3	mass %	84.92	1.53	0.27	-		0.12	-		13.16	$U(Zr)O_2$
	mol. %	29.60	1.39	0.40			0.35			68.26	
	mol. % MeO_x	93.26	4.38	1.27			1.09				
P4	mass %	32.00	21.87	43.34	1.45	0.73	0.35	0.27	-		$(Zr,U)Fe_2$
	mol. %	11.13	19.85	64.26	2.30	1.02	1.02	0.41			
P5	mass %	14.06	35.93	46.28	2.09	0.56	0.80	0.28	-		$Zr(U)Fe_2$
	mol. %	4.33	28.86	60.72	2.94	0.69	2.08	0.38			
P6	mass %	20.50	32.37	44.07	1.90	0.69	0.14	0.32	-		$Zr(U)Fe_2$
	mol. %	6.68	27.52	61.20	2.84	0.92	0.40	0.45			
P7	mass %	0.99	87.75	-						11.26	α-Zr(O)
	mol. %	0.25	57.61							42.14	
	mol. % MeO_x	0.43	99.57								
P8	mass %	83.91	1.62	-						14.47	$U(Zr)O_2$
	mol. %	27.66	1.40							70.95	
	mol. % MeO_x	95.20	4.80								
P9	mass %	21.11	32.69	42.70	2.05	0.55	0.56	0.35	-		$Zr(U)Fe_2$
	mol. %	6.89	27.86	59.43	3.06	0.73	1.54	0.49			
P10	mass %	91.27	1.33	7.26	-		0.14	-			$U(Zr)_3Fe$
	mol. %	71.93	2.73	24.40			0.95				
P11	mass %	83.76	2.49	-			0.14	-		13.61	$U(Zr)O_2$
	mol. %	28.50	2.21				0.40			68.88	
	mol. % MeO_x	91.61	7.11				1.28				
P12	mass %	17.84	34.83	44.07	2.04	0.55	0.31	0.36	-		$Zr(U)Fe_2$
	mol. %	5.71	29.10	60.15	2.98	0.71	0.84	0.50			

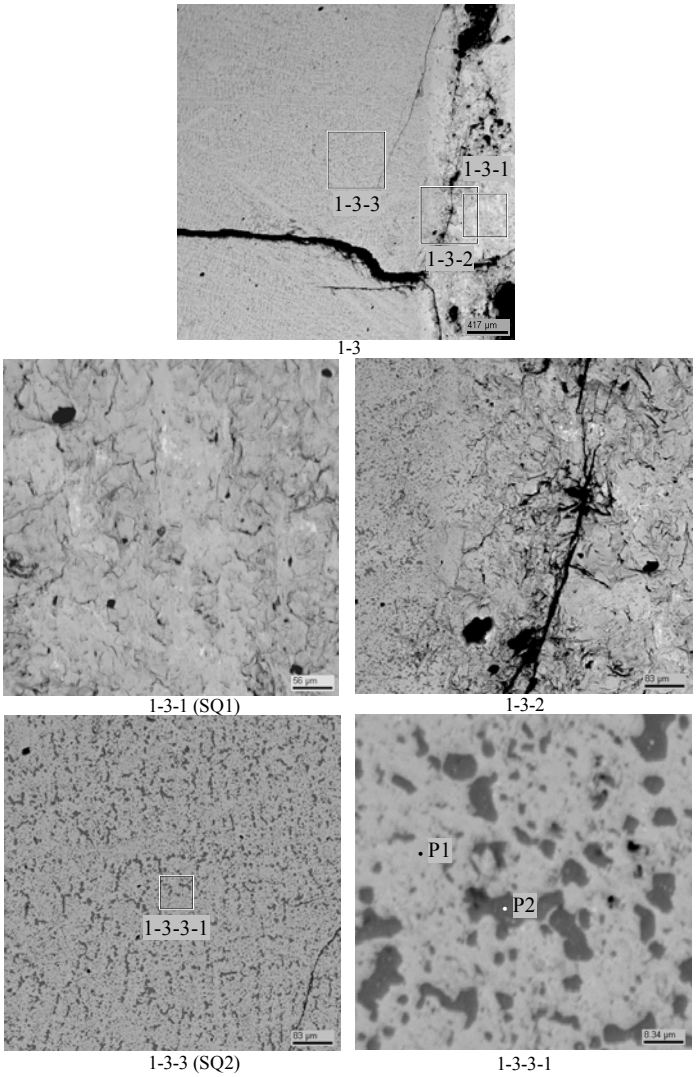

Fig. 2.13 – Micrographs of region 1-3

Table 2.10

EDX data for region 1-3

No.		U	Zr	Fe	Cr	Ni	Si	Mn	Mo	~O	Phase
SQ1	mass %	70.61	4.66	0.86	-		0.21	-		23.65	$U(Zr)O_2$
	mol. %	16.05	2.76	0.83			0.41			79.94	
	mol. % MeO_x	79.99	13.78	4.16			2.06				
SQ2	mass %	67.90	25.12	0.36	-		0.13	-		6.50	-
	mol. %	29.17	28.15	0.65			0.47			41.55	
	mol. % MeO_x	49.90	48.17	1.12			0.81				
P1	mass %	73.90	12.13	0.30	-		0.14	-		13.54	$U(Zr)O_2$
	mol. %	23.89	10.23	0.42			0.38			65.09	
	mol. % MeO_x	68.42	29.31	1.19			1.08				
P2	mass %	19.03	77.04	0.28	-					3.64	α-Zr(O)
	mol. %	6.91	72.98	0.43						19.68	
	mol. % MeO_x	8.60	90.86	0.54							

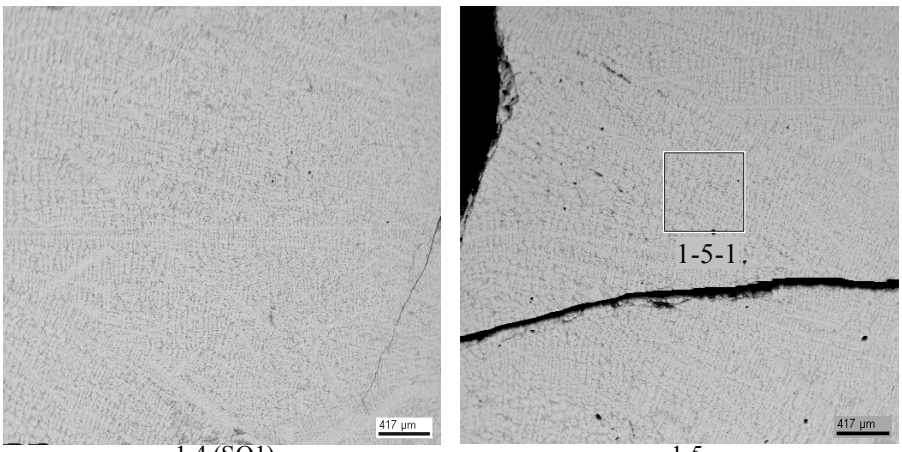

1-4 (SQ1) 1-5

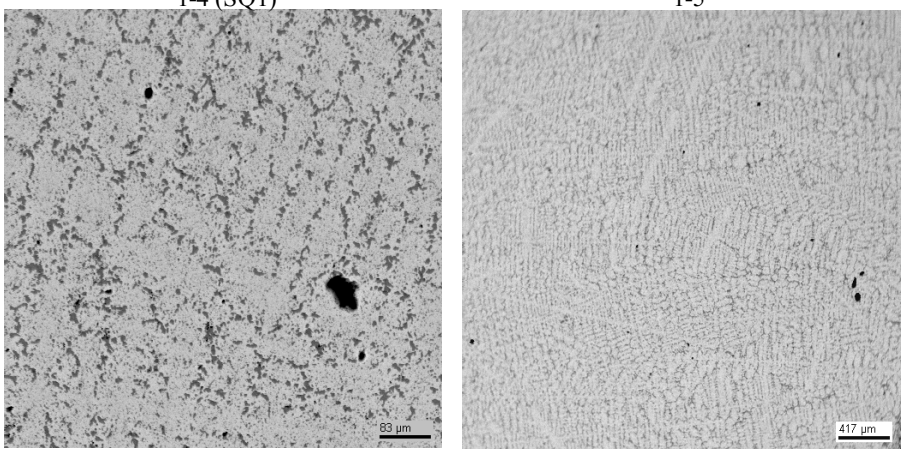

1-5-1 2 (SQ2)

Fig. 2.14 – Micrographs of regions 1-4, 1-5 and 2

Table 2.11

EDX data for regions 1-4 and 2

No.		U	Zr	Fe	Cr	Ni	Si	Mn	Mo	~O	Phase
SQ1	mass %	64.80	24.15	0.37	-		0.10	-		10.58	-
	mol. %	22.53	21.91	0.56			0.30			54.71	
	mol. % MeO_x	49.74	48.37	1.23			0.66				
SQ2	mass %	62.25	24.09	0.49	0.18	-				12.99	-
	mol. %	19.37	19.57	0.65	0.26					60.15	
	mol. % MeO_x	48.62	49.10	1.64	0.64						

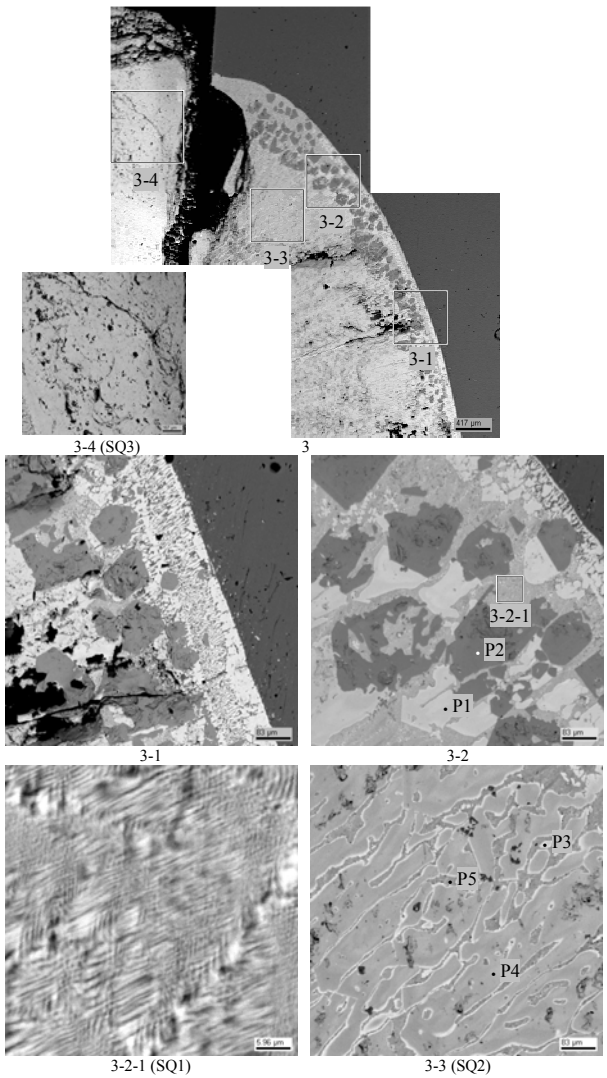

Fig. 2.15 – Micrographs of region 3

Table 2.12

EDX data for region 3

No.		U	Zr	Fe	Cr	Ni	Si	Mn	Mo	~O	Phase
SQ1	mass %	41.14	2.20	52.63	2.16	0.79	0.33	0.39	0.35	-	Eutectic
	mol. %	14.20	1.98	77.44	3.41	1.11	0.96	0.59	0.30		
SQ2	mass %	41.60	11.77	43.29	1.25	0.83	0.45	0.34	0.48	-	-
	mol. %	15.27	11.28	67.75	2.10	1.24	1.39	0.54	0.44		
SQ3	mass %	62.96	15.31	-	0.31	-	-	-	-	21.42	$(U,Zr)O_2$
	mol. %	14.89	9.44	-	0.34	-	-	-	-	75.33	
	mol. % MeO_x	60.35	38.29	-	1.36	-	-	-	-		
P1	mass %	50.04	8.20	39.77	0.67	0.82	0.30	0.21	-		$U(Zr)Fe_{2.5}$
	mol. %	19.95	8.53	67.59	1.22	1.32	1.03	0.36			
P2	mass %	8.70	26.06	62.03	1.64	0.80	0.78	-			$Zr(U)Fe_{3.5}$
	mol. %	2.43	18.97	73.77	2.09	0.90	1.84				
P3	mass %	51.52	7.44	39.24	0.66	0.63	0.21	0.29	-		$U(Zr)Fe_{2.5}$
	mol. %	20.87	7.86	67.76	1.23	1.04	0.73	0.50			
P4	mass %	40.07	14.56	42.84	0.89	0.93	0.50	0.21	-		$(U,Zr)Fe_{2.5}$
	mol. %	14.64	13.88	66.72	1.49	1.38	1.54	0.33			
P5	mass %	42.63	1.65	52.28	2.24	0.72	0.13	0.35	-		~SQ1
	mol. %	14.93	1.51	78.04	3.60	1.02	0.38	0.53			

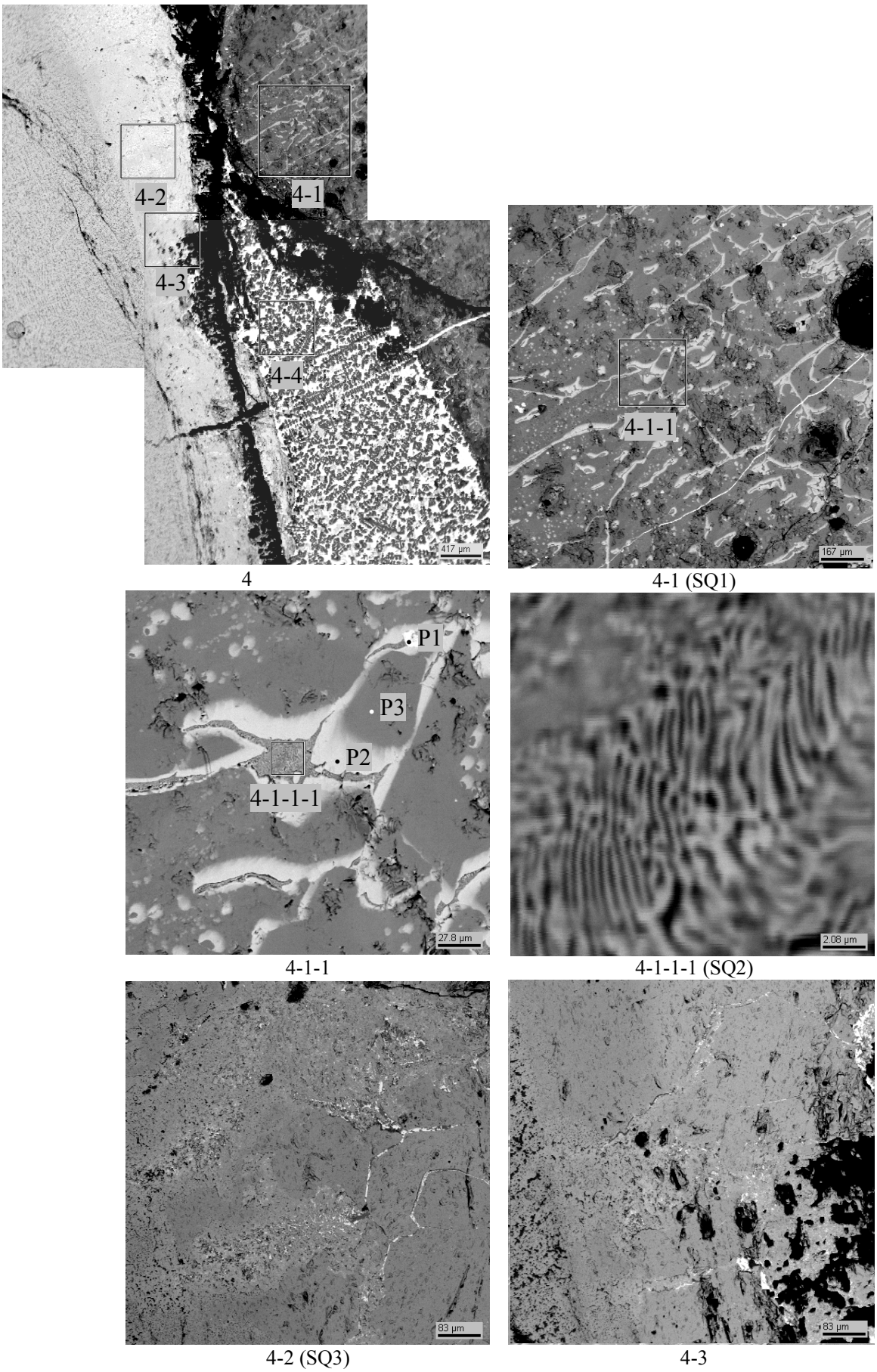

4 | 4-1 (SQ1)

4-1-1 | 4-1-1-1 (SQ2)

4-2 (SQ3) | 4-3

Fig. 2.16 – Micrographs of region 4

Table 2.13

EDX data for region 4

No.		U	Zr	Fe	Cr	Ni	Si	Mn	Mo	~O	Phase
SQ1	mass %	31.46	18.55	41.03	1.24	0.67	0.68	0.32	-	6.05	-
	mol. %	8.73	13.43	48.54	1.58	0.75	1.59	0.38		24.99	
	mol. % MeO_x	11.64	17.91	64.71	2.11	1.00	2.12	0.51			
SQ2	mass %	42.15	1.30	50.63	3.86	1.15	-	0.32	0.59	-	Eutectic
	mol. %	14.71	1.18	75.31	6.17	1.63		0.49	0.51		
SQ3	mass %	74.36	9.98	1.48	-		0.18	-		14.00	$(U,Zr)O_2$
	mol. %	23.50	8.23	1.99			0.48			65.80	
	mol. % MeO_x	68.70	24.07	5.82			1.41				
SQ4	mass %	52.06	19.33	27.58	0.79	-	0.24	-			-
	mol. %	23.07	22.35	52.09	1.61		0.89				
SQ5	mass %	83.68	3.52	12.27	-	0.53	-				-
	mol. %	56.80	6.24	35.49		1.46					
P1	mass %	83.51	0.64	1.85	-		0.18	-		13.82	$U(Fe,Zr)O_2$
	mol. %	27.82	0.56	2.62			0.52			68.49	
	mol. % MeO_x	88.28	1.77	8.32			1.64				
P2	mass %	59.96	3.34	34.57	0.96	0.72	0.16	0.29	-		$U(Zr)Fe_2$
	mol. %	26.54	3.85	65.22	1.95	1.30	0.60	0.55			
P3	mass %	26.49	24.46	46.19	1.25	0.88	0.41	0.33	-		$Zr(U)Fe_2$
	mol. %	8.79	21.18	65.34	1.90	1.18	1.14	0.47			
P4	mass %	95.30	0.49	4.21	-						U_6Fe
	mol. %	83.22	1.11	15.67							
P5	mass %	59.48	5.59	33.62	-	1.31	-				$U(Zr)Fe_2$
	mol. %	26.71	6.55	64.35		2.39					
P6	mass %	27.02	27.02	43.69	0.92	1.01	-	0.33	-		$Zr(U)Fe_2$
	mol. %	9.21	24.02	63.45	1.44	1.40		0.49			
P7	mass %	17.50	33.39	45.83	1.97	0.59	0.42	0.29	-		$Zr(U)Fe_2$
	mol. %	5.53	27.55	61.77	2.86	0.76	1.14	0.40			

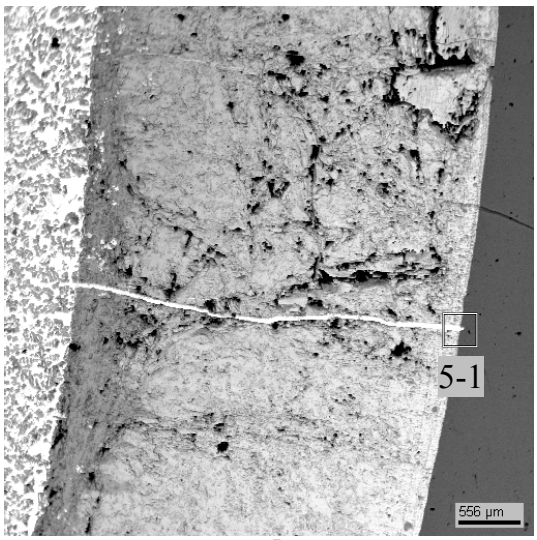

5

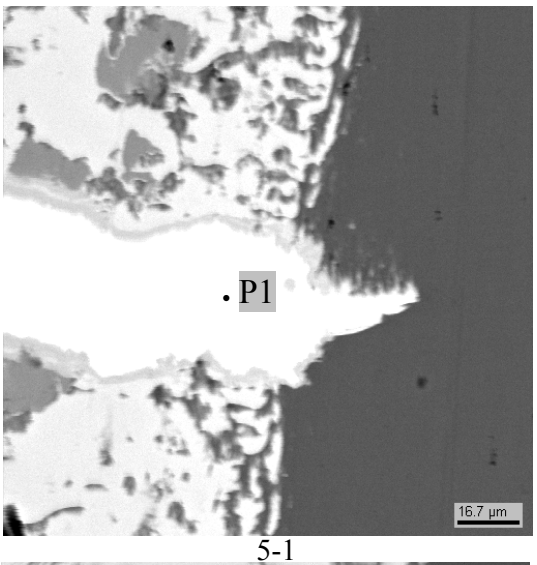

5-1

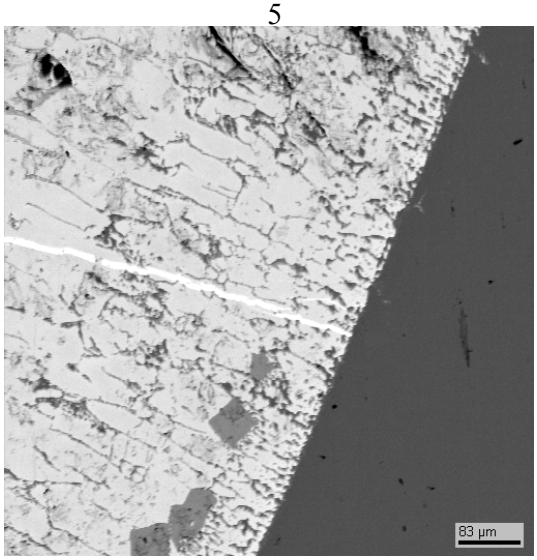

6

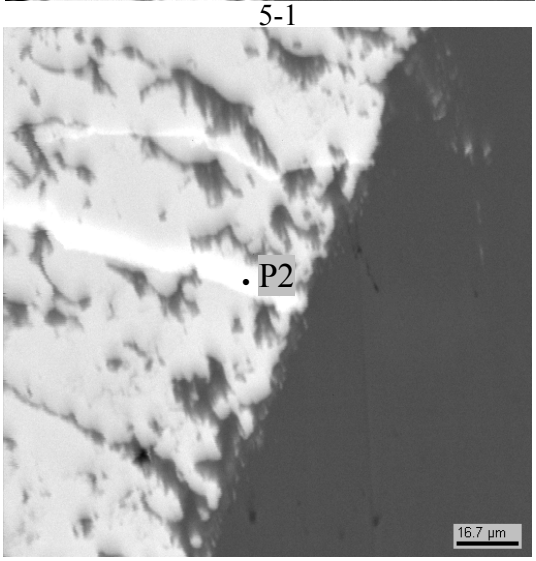

6-1

Fig. 2.17 – Micrographs of regions 5 and 6

Table 2.14

EDX data for regions 5 and 6

No.		U	Zr	Fe	Cr	Ni	Si	Mn	Mo	~O	Phase
P1	mass %	82.82	2.78	13.66	-	0.56	0.17	-			$U(Zr)_{1.5}Fe$
	mol. %	54.47	4.77	38.29		1.51	0.96				
P2	mass %	82.57	1.90	14.80	0.15	0.46	0.11	-			$U(Zr)_{1.5}Fe$
	mol. %	53.57	3.22	40.92	0.45	1.21	0.63				

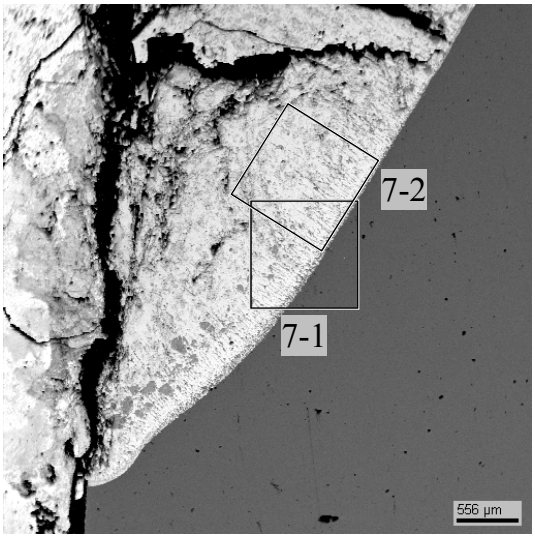

7

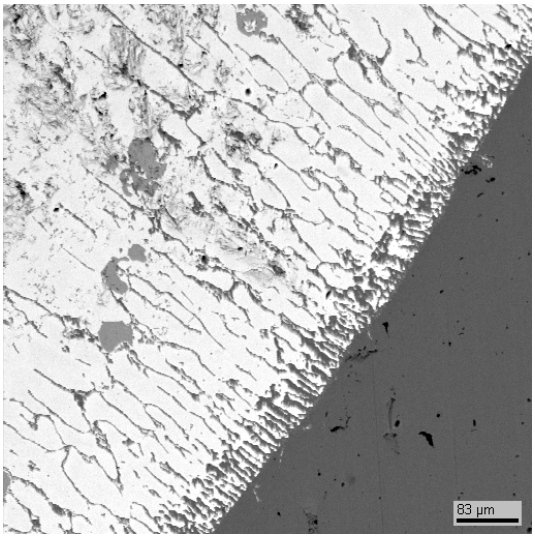

7-1

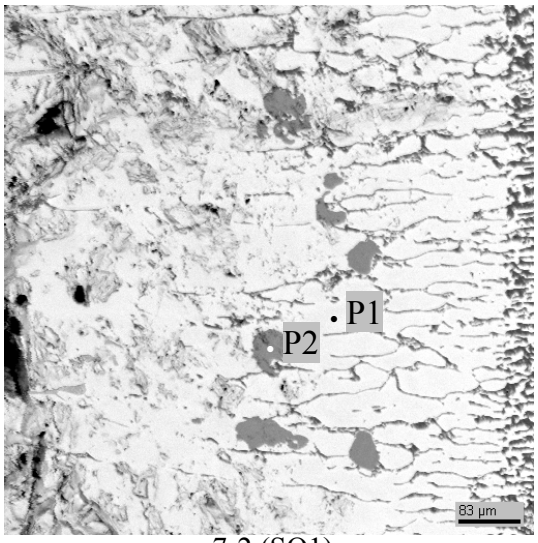

7-2 (SQ1)

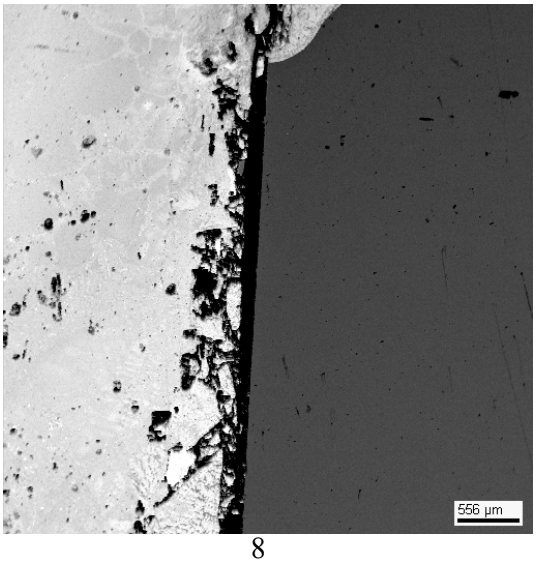

8

Fig. 2.18 – Micrographs of regions 7 and 8

Table 2.15

EDX data for region 7											
No.		**U**	**Zr**	**Fe**	**Cr**	**Ni**	**Si**	**Mn**	**Mo**	**~O**	**Phase**
SQ1	mass %	45.01	5.99	45.57	1.58	0.74	0.54	0.23	0.34	-	-
	mol. %	16.58	5.76	71.54	2.66	1.11	1.68	0.37	0.31		
P1	mass %	54.50	5.73	37.95	0.68	0.72	0.21	0.21	-		$U(Zr)Fe_{2.5}$
	mol. %	22.71	6.24	67.41	1.29	1.22	0.75	0.38			
P2	mass %	13.97	23.32	59.15	1.80	0.81	0.58	0.38	-		$Zr(U)Fe_{3.5}$
	mol. %	4.05	17.63	73.07	2.38	0.95	1.44	0.47			

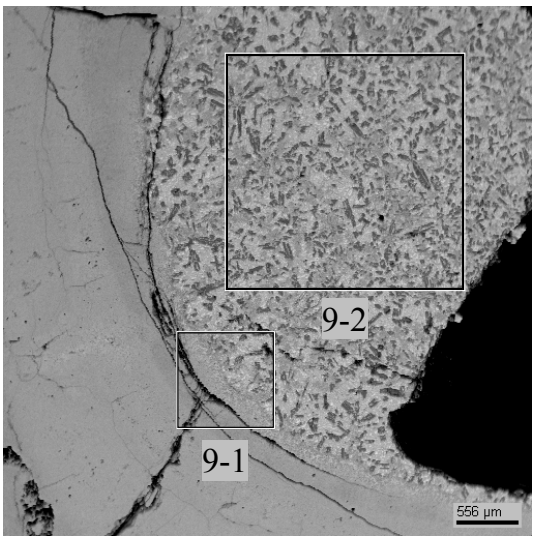

9

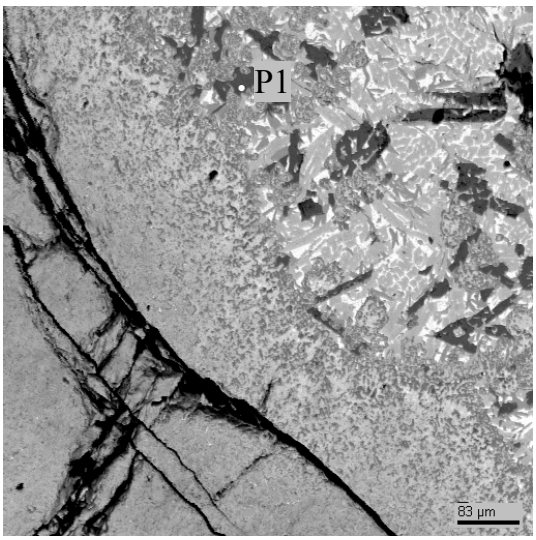

9-1

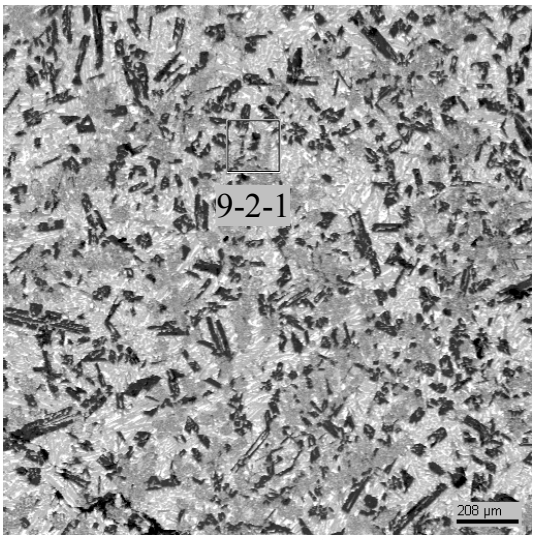

9-2 (SQ1)

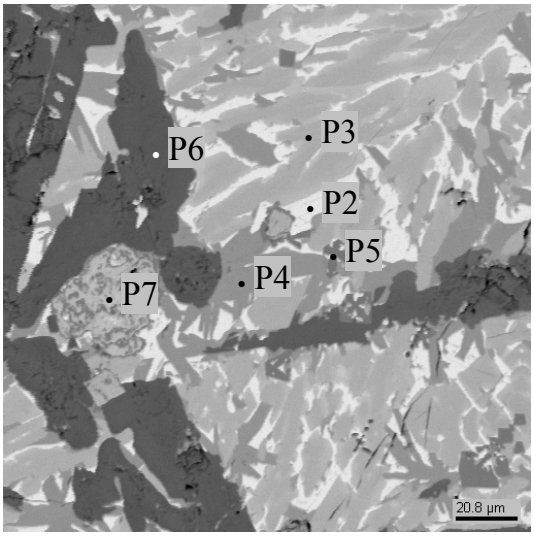

9-2-1

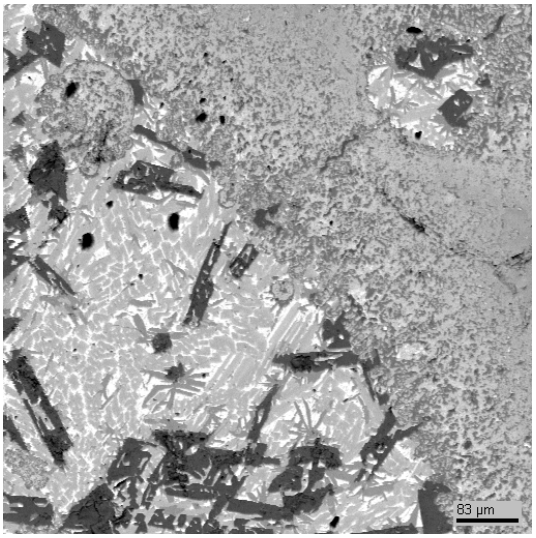

10

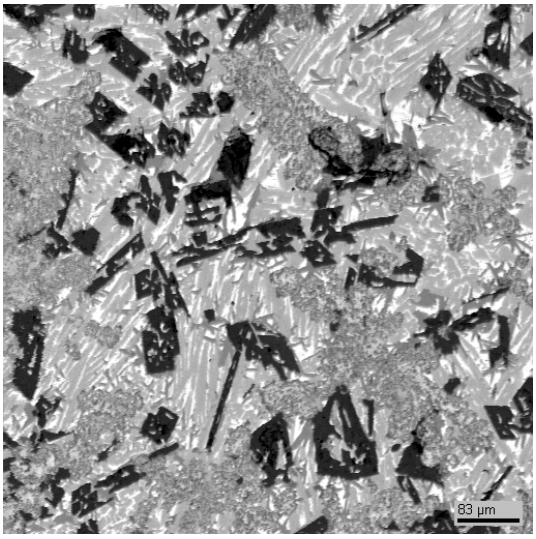

11 (SQ2)

Fig. 2.19 – Micrographs of regions 9-11

Table 2.16

EDX data for regions 9-11

No.		U	Zr	Fe	Cr	Ni	Si	Mn	Mo	~O	Phase
SQ1	mass %	53.10	24.74	21.25	0.17	0.41	0.33	-			-
	mol. %	24.88	30.24	42.42	0.37	0.79	1.30				
SQ2	mass %	53.20	24.66	21.03	0.21	0.54	0.35	-			-
	mol. %	24.94	30.16	42.01	0.45	1.03	1.40				
P1	mass %	8.26	32.24	32.69	4.57	0.30	1.02	-	1.47	19.45	$ZrFe_2(O)$
	mol. %	1.49	15.14	25.08	3.77	0.22	1.56		0.66	52.09	
	mol. % MeO_x	3.10	31.61	52.35	7.86	0.45	3.25		1.37		
P2	mass %	95.22	0.44	4.34	-						$U(Zr)_6Fe$
	mol. %	82.90	1.01	16.09							
P3	mass %	55.71	27.88	15.52	-	0.89	-				$(U,Zr)_2Fe$
	mol. %	28.10	36.70	33.38		1.82					
P4	mass %	43.01	27.17	29.20	-				0.62	-	(Zr,U)Fe
	mol. %	17.93	29.56	51.88					0.64		
P5	mass %	22.69	55.59	21.32	-	0.40	-				$(Zr,U)_2Fe$
	mol. %	8.72	55.74	34.92		0.62					
P6	mass %	8.13	40.86	48.63	0.68	0.39	1.32	-			$ZrFe_2(O)$
	mol. %	2.40	31.56	61.34	0.92	0.47	3.31				
P7	mass %	82.35	1.94	3.01	-					12.69	$U(Zr,Fe)O_2$
	mol. %	28.49	1.75	4.44						65.32	
	mol. % MeO_x	82.15	5.05	12.80							

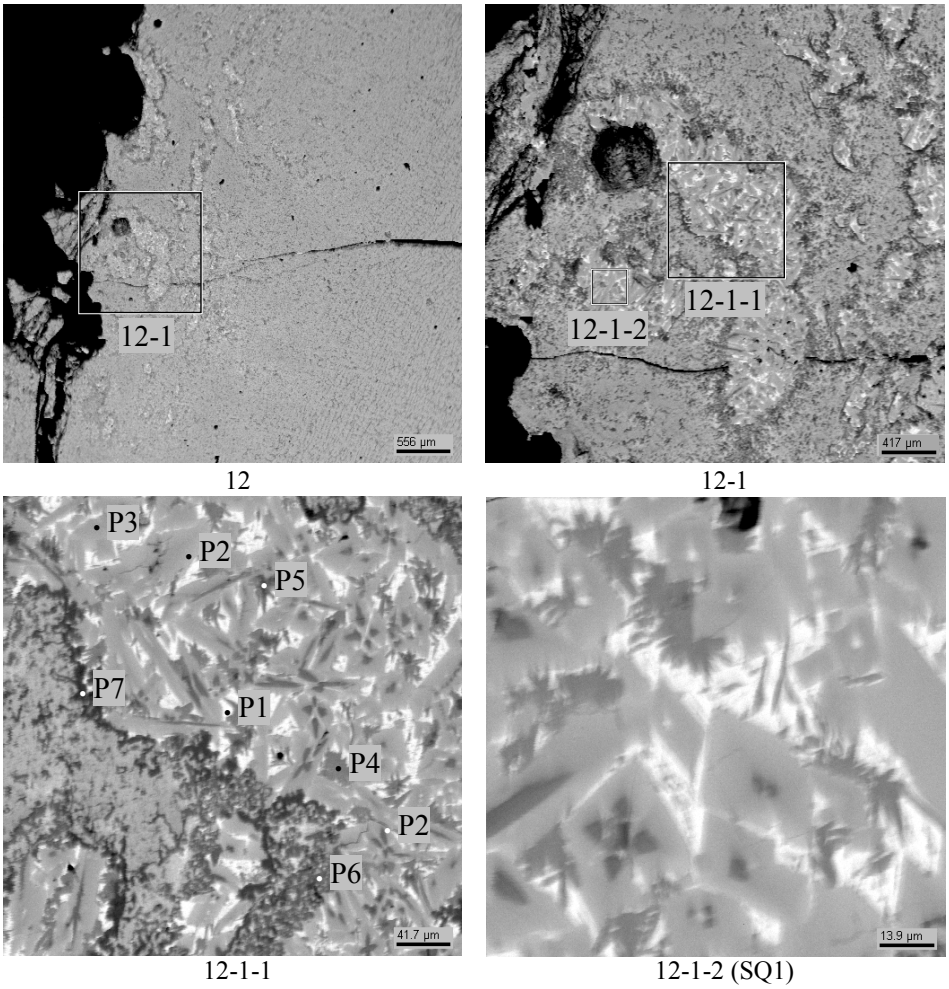

Fig. 2.20 – Micrographs of region 12

Table 2.17

EDX data for region 12

No.		U	Zr	Fe	Cr	Ni	Si	Mn	Mo	~O	Phase
SQ1	mass %	59.64	24.51	15.11	-	0.45	0.29	-			-
	mol. %	31.01	33.25	33.49		0.96	1.29				
P1	mass %	91.84	2.41	5.75	-						$U(Zr)_4Fe$ Mixture?
	mol. %	74.88	5.13	20.00							
P2	mass %	57.30	26.87	15.36	-	0.47	-				$(Zr,U)Fe_2$
	mol. %	29.41	35.99	33.62		0.99					
P3	mass %	53.41	30.54	15.35	-	0.42	0.27	-			$(Zr,U)Fe_2$
	mol. %	26.37	39.34	32.30		0.84	1.14				
P4	mass %	43.27	27.92	27.55	0.76	-			0.50	-	Zr(U)Fe Mixture?
	mol. %	18.16	30.58	49.28	1.47				0.52		
P5	mass %	32.75	51.11	12.33	-	0.76	3.05	-			$Zr(U)_3Fe$
	mol. %	13.23	53.86	21.23		1.25	10.44				
P6	mass %	31.25	51.49	16.70	-	0.37	0.19	-			$Zr(U)_3Fe$
	mol. %	13.03	56.00	29.67		0.62	0.68				
P7	mass %	2.80	90.04	1.90	-					5.26	α-Zr(O)
	mol. %	0.86	72.48	2.50						24.15	
	mol. % MeO_x	1.14	95.56	3.30							

2.5. Specimen metallography

Metallographic investigations and measurements were carried out on the specimen longitudinal section. Direct measurements were made using the MBS-9 stereoscopic microscope at magnifications from x10 to x50 and at x100, and the METALLUX metallographic microscope at x100 and x400. The scale factor of micrometer screw and object plate of microhardness meter is 0,01 mm (10 μm). The measurement error is ±10 μm; it was determined with stage micrometer. The results of measuring profile of the steel specimen after the test (Figs. 2.21, 2.22), profilograms of the boundary of the corium/steel interaction zone, of the boundary between two regions of the interaction zone (lines 2 and 4, Fig. 2.22), as well as the boundary profilogram (line 3, Fig. 2.22) for the zone of corium thermal influence on steel were constructed. Fig. 2.23 shows these boundaries in the following coordinates: specimen Ø along the X-line, steel specimen height along the Y-line. The results of measurements are given in Fig. 2.22 a, b.

Template grinding and polishing was carried out in accordance with standard methodology. In order to reveal the microstructure, the prepared microsection was etched and quality controlled using the metallographic microscopes. The etchants for austenite and pearlite steels [12] were used, they made it possible to reveal the macro- and microstructure in the zone of high-temperature impact of molten corium on steel, and identify steel microstructure.

The surface of sections was photographed by a NIKON digital camera through MBS-9 stereoscopic microscope at magnifications from x10 up to x100 and the METALLUX metallographic microscope at x100, x200 and x400 magnifications. The revealed macrostructure the steel specimen longitudinal section made it possible to identify and area between lines 2 and 3 (Fig. 2.21), in which macro- and microstructure had changed. Figs. 2.24 and 2.25 contain fragments of images showing macrostructure of the steel specimen regions. Fig. 2.26 offers fragments of images showing microstructure of the regions (shown in Fig. 2.25 c, d) in the zone of thermal impact of molten corium and in the zone of transition (Fig. 2.26 e) to the initial pearlitic structure of steel.

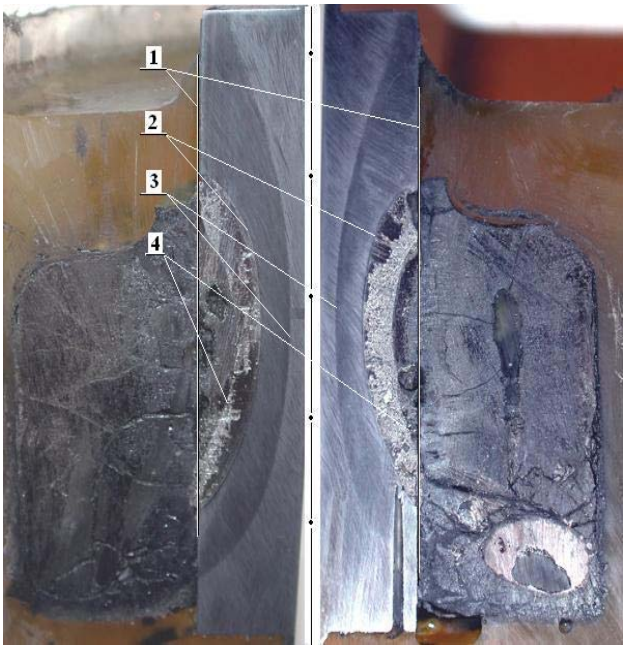

1 – conventional lateral surface of the initial steel specimen; 2 – corium/steel interaction zone boundary; 3 – boundary of the zone of molten corium thermal impact on steel structure; 4 – boundary between two parts of the interaction zone.

Fig. 2.21 – Longitudinal section of the 'corium-steel specimen' block

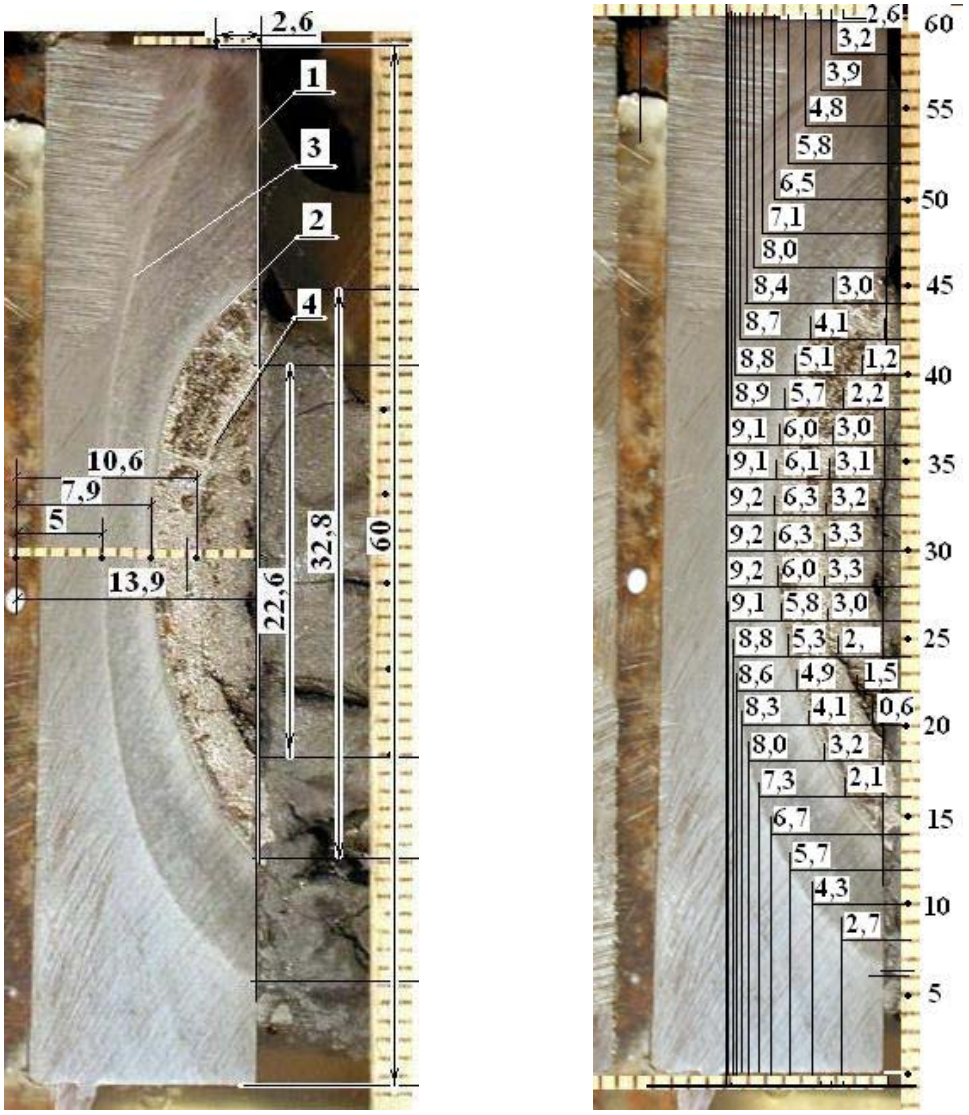

а) б)

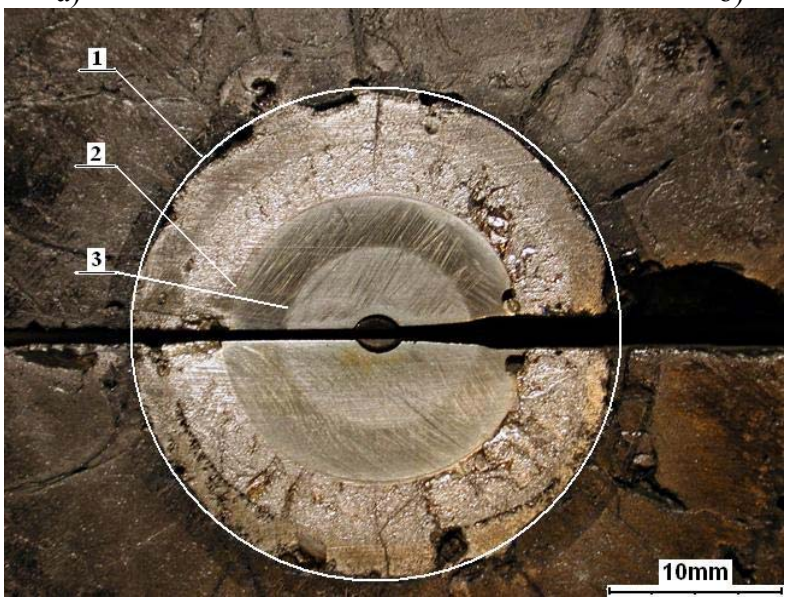

c)

Fig.2.22 – Longitudinal (a, b) and transverse (c) sections of the polished section from the zone of corium/steel interaction

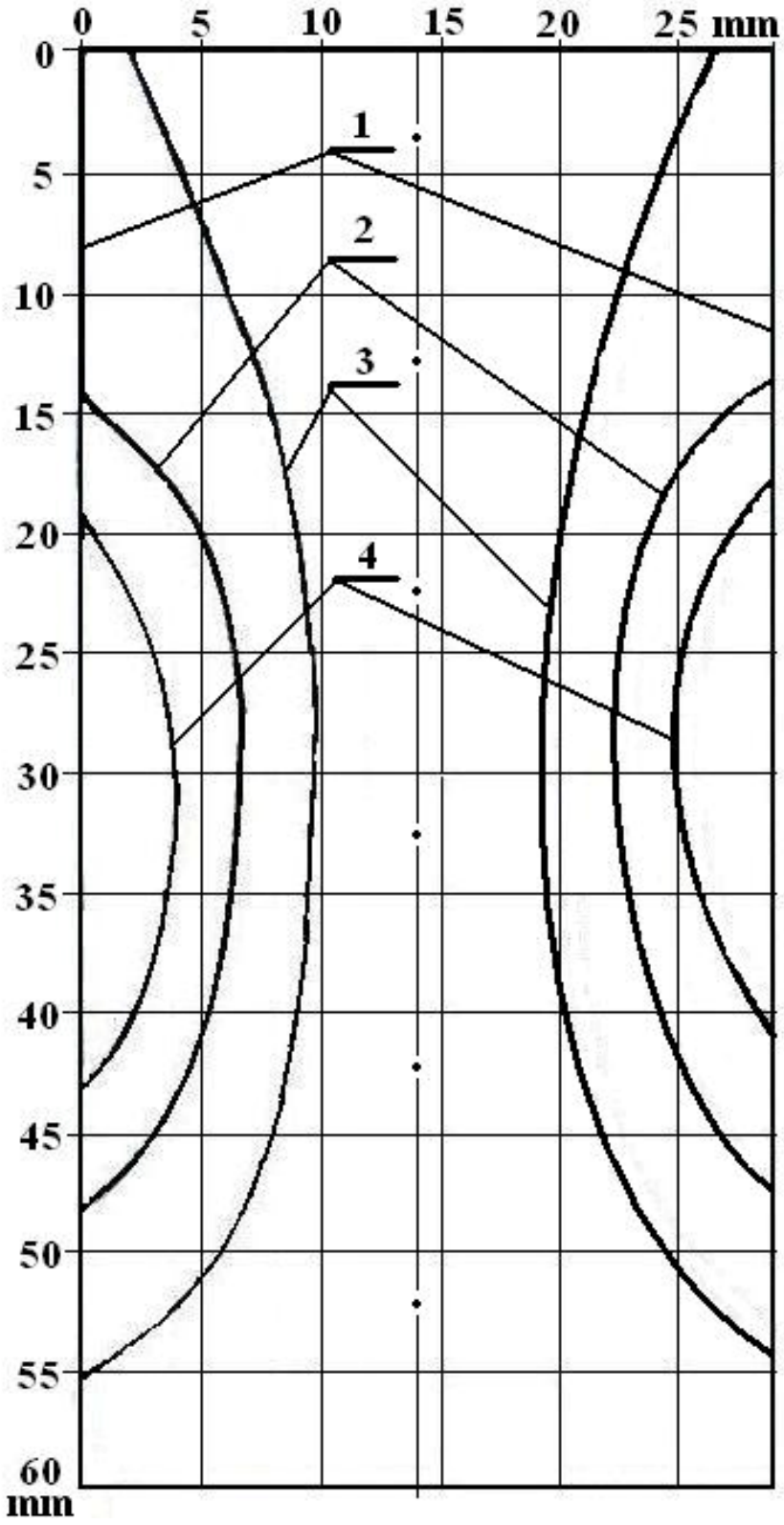

1 – conventional lateral surface of the initial steel specimen;
2 – corium/steel interaction zone boundary;
3 – boundary of the zone of molten corium thermal impact on steel structure;
4 – boundary between two parts of the interaction zone.

Fig.2.23 – Position of characteristic boundaries in the specimen

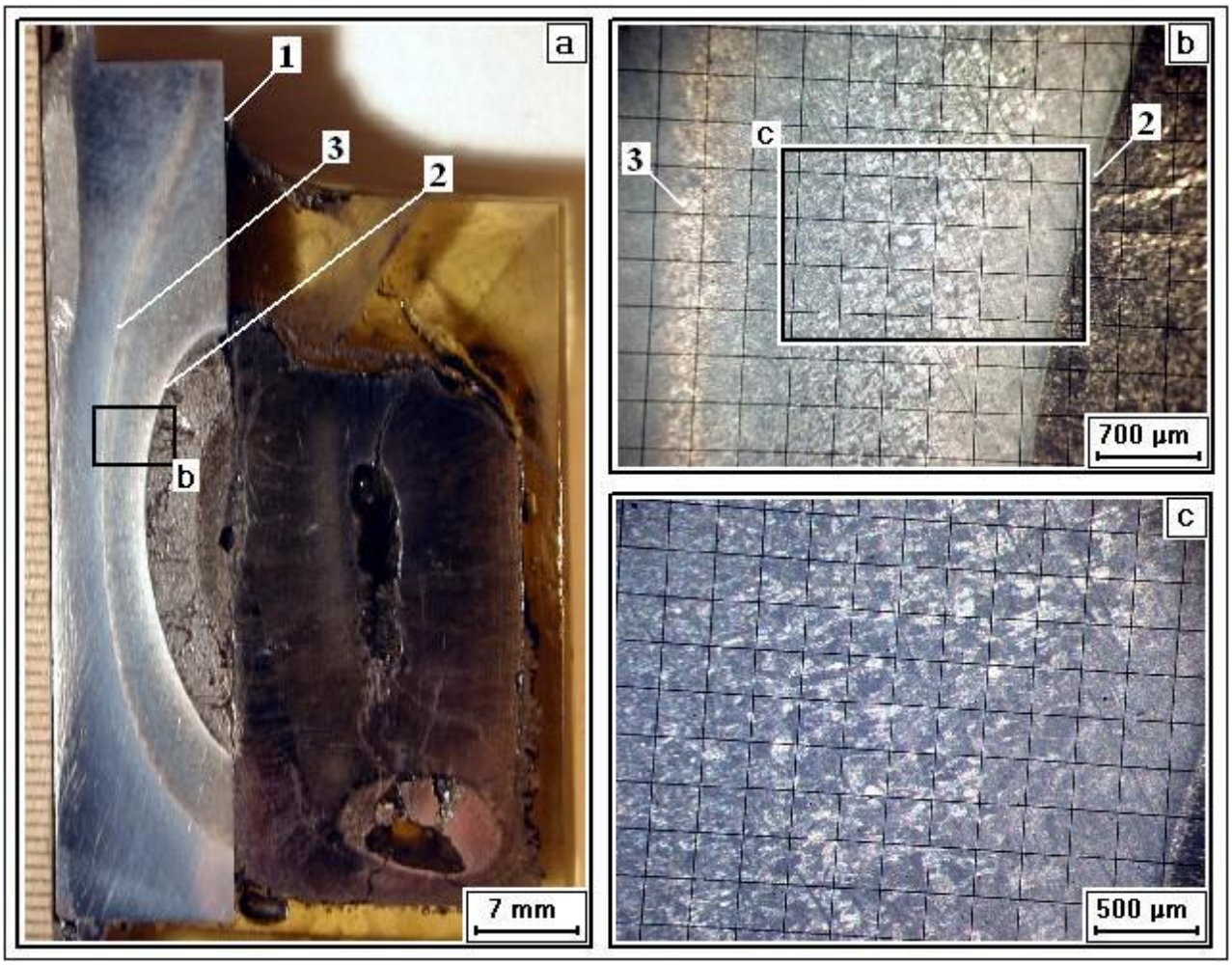

1 – conventional lateral surface of the initial steel specimen;
2 – corium/steel interaction zone boundary;
3 – boundary of the zone of molten corium thermal impact on steel structure.

Fig.2.24 – Half of the longitudinal section and macrostructure fragments of the steel specimen

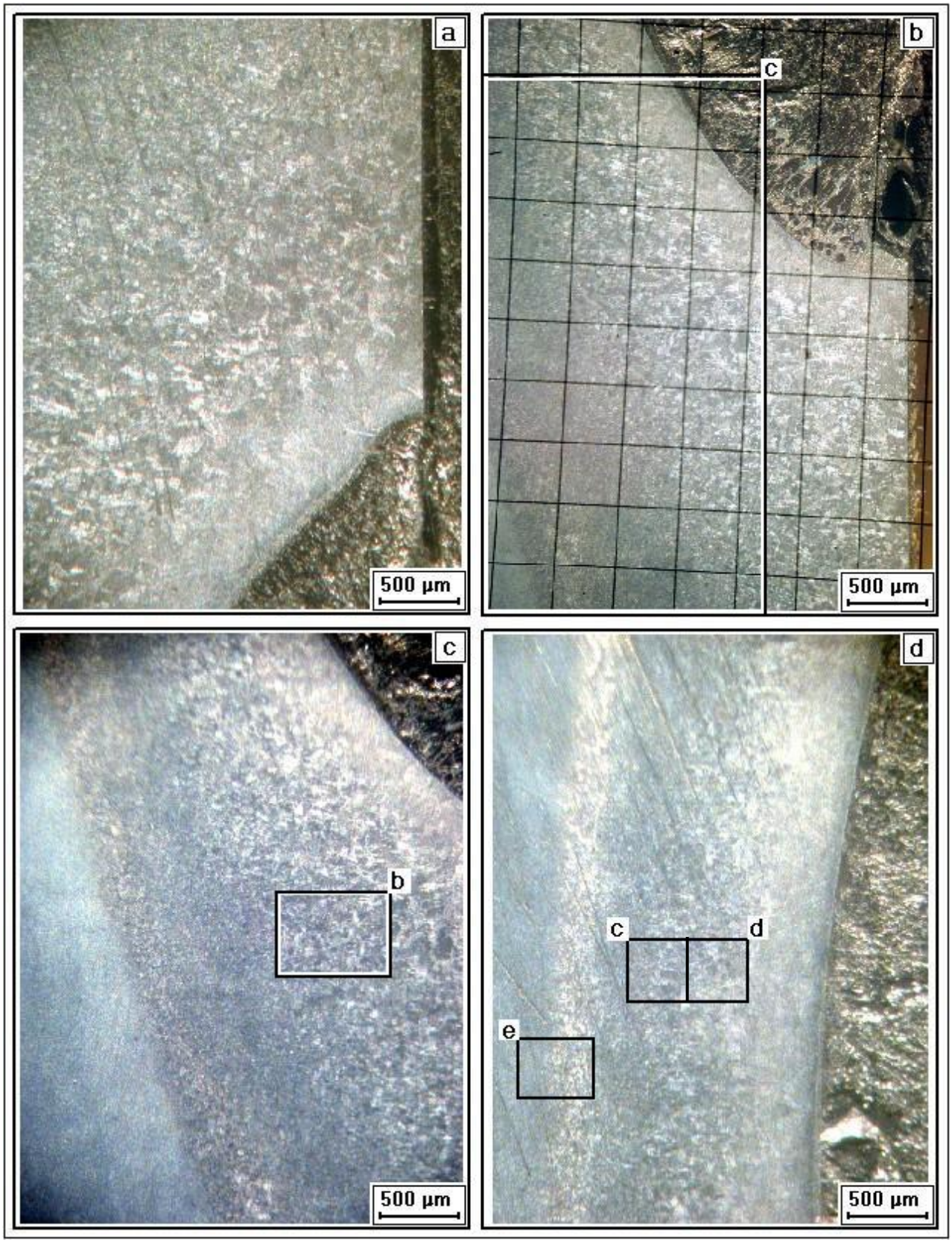

a – zone upper part; b, c – zone lower part; d – zone central part with polished section regions used for microstructural studies (see Fig. 2.26 b-e)

Fig.2.25 – Steel macrostructure in the zone of molten corium thermal impact

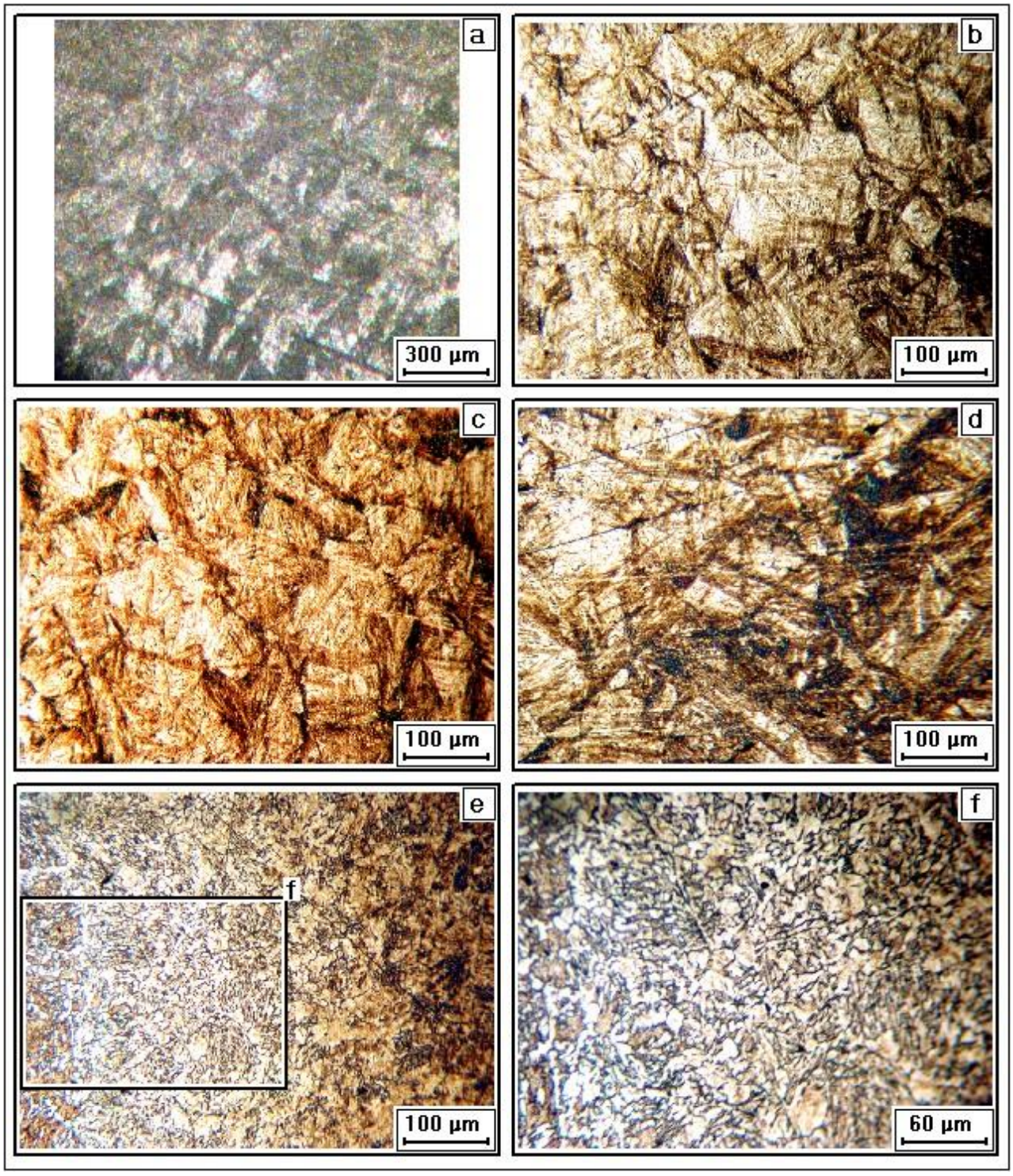

Fig.2.26 – Steel microstructure (b-f) in the zone of molten corium thermal impact

Macrostructurally, the steel between lines 2 and 3 (Fig. 2.21) contains large grains (grain size is 1 - 5 points). Steel microstructure in this area is of mixed type, that is, ferritic + ferrite-pearlitic with different degrees of pearlite dispersivity and shape (Fig. 2.26). Such a structure speaks in favour of heating above the critical point Ac_3 and, consequently, of the complete recrystallization of steel, while line 3 (Fig. 2.21) marks the temperature front boundary which goes to the maximum depth of 9.2 mm from the specimen lateral surface.

Presumably, the entire zone of thermal impact is characterized by diffusion of carbon and chromium from hot to cold layers. This is confirmed by microstructure of the layer (region e in

Fig.2.25). This is lamellar pearlite that evidences the eutectoid composition, which is richer in carbon than the initial steel. Diffusion of alloying elements into this region may influence temperature of the eutectoid transformation, but since their quantity in the vessel steel is not big, it may be supposed that the temperature of eutectoid formation (in comparison with the Fe-Fe_3C constitution diagram) [13, 14] will not change much and amount to 727ºC.

2.6. Determination of oxygen by the method of carbothermal reduction

In order to specify oxygen content in the fused products and in the interaction zone, the analytical method of carbothermal reduction (CTR) was applied to samples.

The method is based on the release of oxygen as part of CO–CO_2 from the molten sample at the reduction of the sample with carbon of the crucible, followed by the analysis of the gaseous phase and determining the mass loss. The analytical technique envisages use of individual porous graphite crucibles for each sample. The crucible holding one sample and Ni fusing agent, as well as powdered graphite, is small (Ø 10 – 15 mm) and therefore does not require long degassing. Adding of the powdered carbon and fusing agent helps to reduce CO_2 formation to the minimum and improve kinetic and thermodynamic conditions of gas release from samples. The analysis of some systems has shown that the introduction of fusing agent decreased the completeness of reduction, as these systems reduced without Ni fusing agent. When reproducibility of thermogram of the reference crucible heating is ensured by thermogram of heating the crucible with sample, accuracy of the analysis is sufficiently high. A general flowchart of the CTR facility is given in Fig. 2.27.

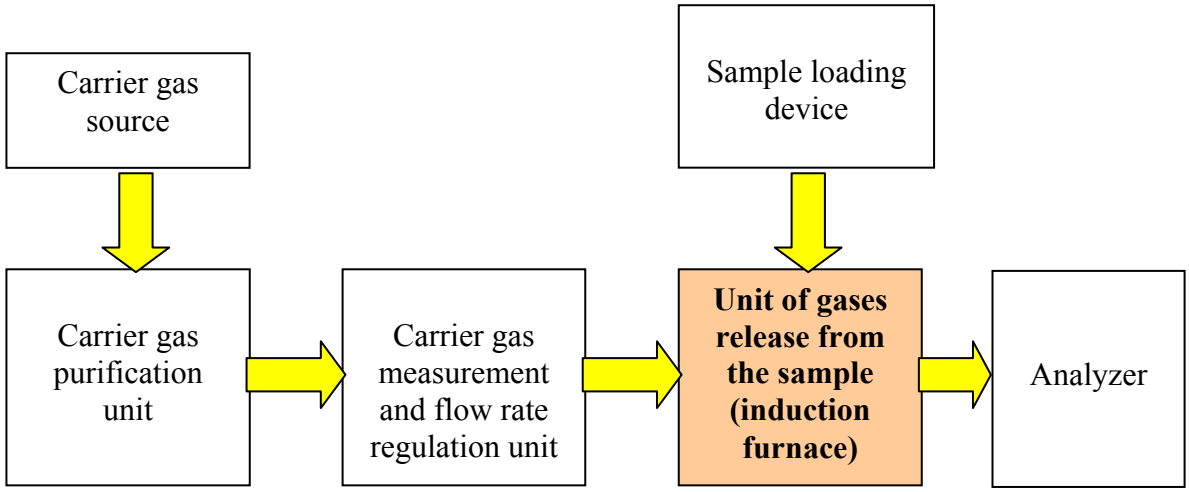

Fig. 2.27 – Flowchart of the facility for CTR in flowing carrier gas

The flowchart shows the facility to be composed of three main parts:

- Carrier gas preparation system including purification and regulations units,
- Unit of gases release from the sample (furnace) with a sampling device,
- Gas analyzer.

The analysis employed an induction furnace with the coaxial water-cooled quartz tube, into which the graphite crucible with sample was placed, and a system of carrier gas supply and off gases analysis. Fig. 2.28 shows the experimental cell and graphite crucible, and Fig. 2.29 offers the furnace diagram.

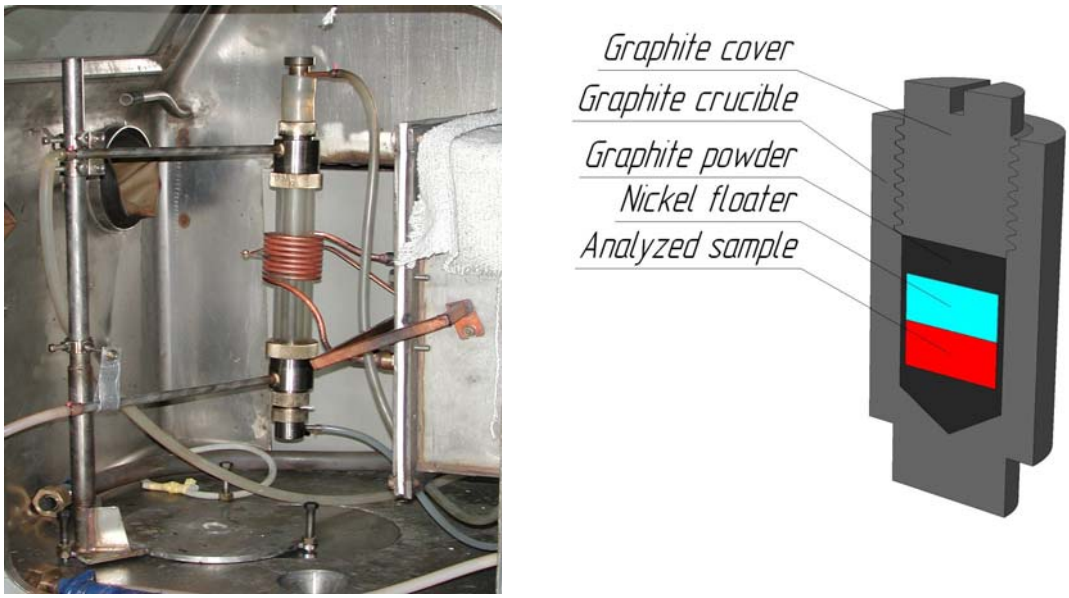

Fig. 2.28 – CTR furnace and graphite crucible in assembly

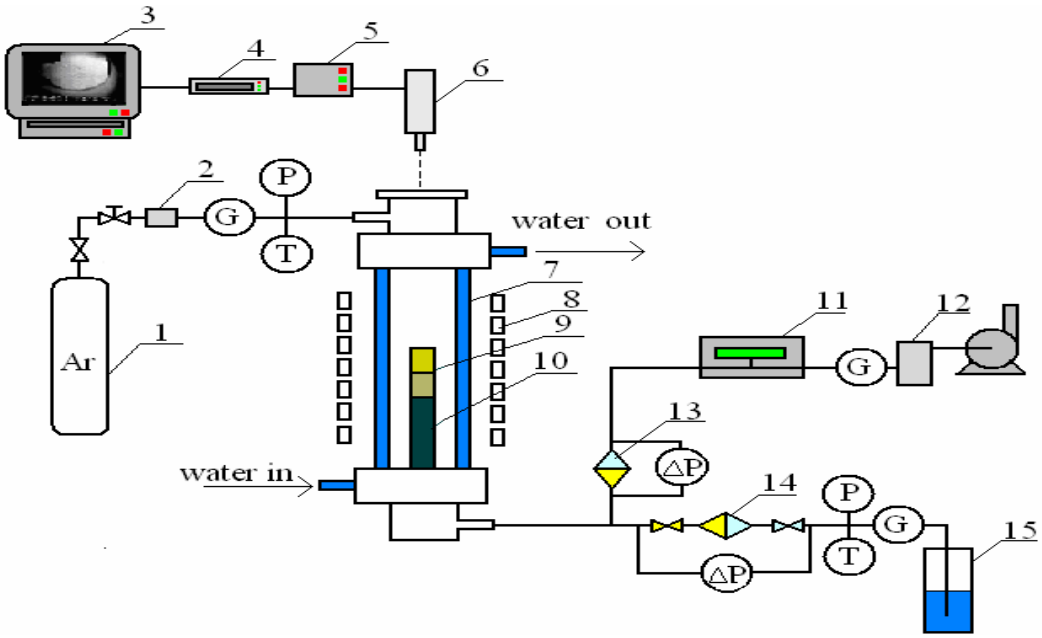

1 – Ar cylinder; 2 – carrier gas purification unit; 3 – monitor/videotape recorder; 4 – device for pasting measurement results into videoframes; 5 – DAS; 6 – pyrometer coupled with video camera; 7 – water-cooled quartz tube of the furnace; 8 – inductor; 9 – crucibles (experimental and reference); 10 – crucible holder; 11 – mass spectrometer; 12 – vacuum vessel (receiver); 13,14 – Petryanov analytical filters (AAF); 15 – sparger with CO_2 – absorbing solution.

Fig. 2.29 – Diagram of a furnace for carbothermal reduction in flowing carrier gas

The analytical procedure included:

1. Reloading of the carrier gas dehumidifier cartridge.
2. Sample weighing (about 0.3 g), mixing with powdered carbon (about 30% of the sample mass), mixture placing into the graphite crucible and fusing agent (Ni) adding (Ni) in an amount equal to 30-100% of the sample mass.
3. Charged crucible weighing.
4. Crucible degassing in a chamber at about 1 mbar.

5. Crucible loading into the furnace.
6. Gas line sealing and switching on of the system for the off gases collecting and analyzing.
7. Furnace blasting with the carrier gas for 3 min to remove air from the system.
8. Quick induction heating of the sample up to 1400°C.
9. CO content measurement in the off gas*.
10. Adjustment of the pyrometer and video camera aimed at the crucible.
11. Crucible smooth heating up to the operational temperature (2300 - 2550°C).
12. Crucible exposure at the operational temperature for 1÷5 min.
13. Heating termination and crucible cooling.
14. Calculation of oxygen content in the sample on the basis of mass deficiency, taking the idle test into account, and of CO quantity.

*) the measurements showed concentration of CO_2 in gas to be not more than 2% for all samples.

Tab. 2.18 summarizes conditions of the analysis.

Table 2.18

Analysis conditions

Parameters	Value
Carrier gas	Ar
Carrier gas flow rate, ml/min	100÷3000
Final content of impurities in the carrier gas, vol. %	Less than 10^{-3}
Crucible operational temperature, °C	2300÷3000
Sample exposure at the operational temperature, min	1÷5
Sample form	Powder or pieces
Fusing agent	Compact Ni

The error of oxygen determination is not more than 3 relative %. When calculating mass deficiency after the test, mass losses of the crucible and cover were taken into account, as well as the amount of oxygen in metallic Ni.

Tab. 2.19 contains the measured oxygen concentrations in samples from MCP-1 and their averaged values used for correcting samples composition.

Table 2.19

Measured oxygen content in samples from MCP-1

Sample	O content, mass %	
	Experimentally obtained value	Averaged value
Above-melt crust	12.10, 12.24, 12.02	12.12
Corium ingot (top)	11.36, 11.28, 11.21	11.28
Corium ingot (bottom)	10.36, 10.32, 10.38, 10.46	10.38
Interaction zone I	0.25, 0.24, 0.22	0.24
Interaction zone II	1.67, 1.65, 1.89	1.72
Metallic body (located in corium ingot)	1.75, 1.79, 1.96	1.83

3. DISCUSSION OF RESULTS

When working MCP-1 out, it was surmised that possible differences from MC6 may be determined by the influence of a single factor, that is, the changed orientation of the interaction interface from horizontal to vertical. The performed posttest analyses have found the differences from MC6 to be significant, while their relation to the above-mentioned factor unobvious. These differences are listed below.

1). IZ composition
In MC6, SEM/EDX has shown the IZ to be composed of (mass %) : 25.6%U-5.4%Zr-64.4%Fe.
In MCP-1, the XRF results have shown the composition of two parts of the IZ to vary within the following limits (mass %) : 36.4...52.4 %U-13.7...14.3 %Zr-32.2...49.1 %Fe(Cr, Ni).
Thus, a significant difference in concentrations is observed for all components of the IZ; the content of Fe has decreased and that of U and Zr has increased.

2). Temperature (T_{int}) at the boundary of the interaction front final position.
In MC6, T_{int}=1120...1200°C, while in MCP-1 T_{int}=1000...1090°C, i.e., T_{int} has decreased by over 100°C.

3). In MC6, the incubation period was approximately 16000 s, while in MCP-1 it was not more than 4000 s, or was absent at all.

The latter difference may be due to the following circumstance: calculations of the specimen temperature condition have shown the heat flux to the specimen from molten corium in MCP-1 to be about 2.0 MW/m^2, while in MC6 q≈1.25 MW/m^2. The specimen surface temperature was higher in MCP-1. The calculated value of this temperature was 1435°C, but in fact it could be higher, as in contrast to all other METCOR tests, the calculations were not based on the direct temperature measurements in the interaction zone. Therefore, thickness of the corium crust on the specimen surface in MCP-1 was significantly smaller, and in combination with a higher temperature at the interaction interface, it all could lead to shortening of the period of the initial liquid phase formation.

The other differences from MC6 are interrelated and can be explained by significantly different composition of molten corium. The composition of charge loaded in MCP-1 was identical to that of corium in MC6, but formation of a thick surface crust has made the melt composition differ from that of the charge. According to the data from Tab. 2.6, and supposing that the crust composition (except for Fe) was constant throughout the test, the index of melt oxidation by the beginning of interaction with the specimen was C-17 in contrast to C-30 in MC-6. The results of MASCA (and GEMINI calculations) show that U and Zr concentrations in the metallic part of the system increase at lower oxidation degrees, other conditions being equal. However, the mass fraction of steel participating in the interaction has also changed in MCP-1 in comparison with MC-6.

To compare composition of the IZ in MCP-1 with composition of the metallic part of the melt that would have formed in a thermodynamically equilibrium system with a degree of oxidation and mass fraction of steel corresponding to conditions of MCP-1, calculations have been performed using the GEMINI code and NUCLEA database. Applicability of GEMINI for calculations of a similar two-liquid system was proved in [15] during the analysis of findings from MASCA. The results of calculations and averaged experimental data from MCP-1 are presented in Tab. 3.1. A comparison showed a noticeable discrepancy, though experimental values are closer to the calculated ones than in the previously conducted MC6...MC8 [16] (Fig. 3.1, 3.2). That is, the results of MCP-1, like the results of the previous tests, confirm the

influence of thermogradient conditions on compositions of the coexisting oxidic and metallic parts of the system.

Table 3.1

Composition of the IZ metallic part

	Composition, mass %			
	U	Zr	Fe(Cr,Ni...)	O
Calculated	57.6	16.6	25.5	0.03
Experimental	43.5	14.0	41.6	0.5

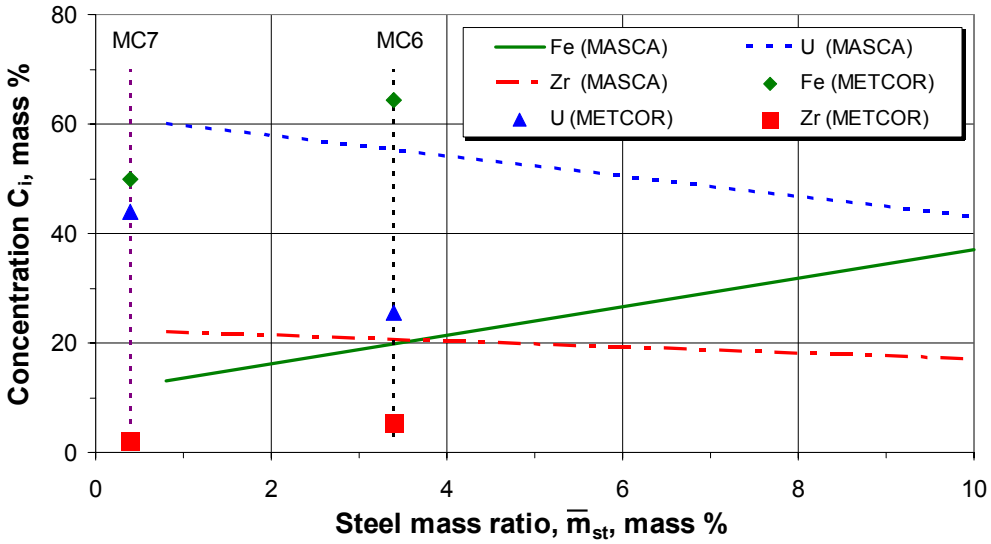

$C_n \approx 30\%$

Fig. 3.1. – Composition of the metallic part of the melt (MASCA) and IZ (METCOR) subject to the mass fraction of steel in the system

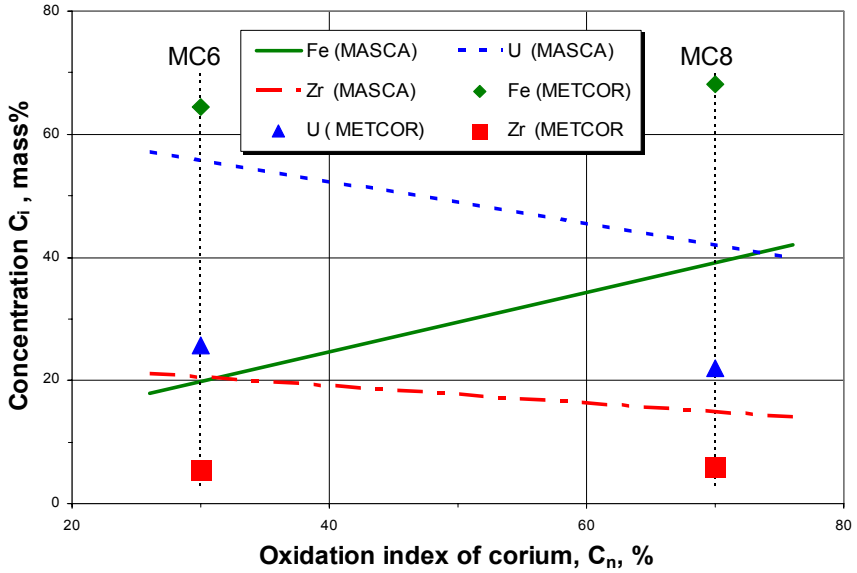

$\overline{m}_{st} \approx 3\%$mass

Fig. 3.2. - Composition of the metallic part of the melt (MASCA) and IZ (METCOR) subject to the melt oxidation index

Thus, the main distinction between the results of MCP-1 and MC6, namely the IZ compositions, can be mainly explained by difference in the degree of molten corium oxidation. To tell the truth, there was no possibility to measure the melt temperature because of a thick surface crust in MCP-1, but even if it differed from the temperature of MC6, it could not have a significant influence. At least, calculations for the MASCA conditions using GEMINI have shown that the change of temperature in a wide range has a weak impact on compositions of the coexisting phases in a two-liquid system.

The difference from MC6 concerning the value of T_{int} at the boundary of the final position of the front of interaction with the specimen is directly linked to the different composition of the IZ. Fig. 3.3 presents the results of MC6...MC9 [16] and MCP-1. Obviously, the value of T_{int} obtained in MCP-1 satisfactorily agrees with the data from the previous tests and, like in MC7 and MC9 with a higher U concentration in the IZ, corresponds to the solidus temperature of the U-Zr-Fe-(O) system. It should be noted that the calculated value of T_{int} has been determined with a bigger error in MCP-1 than in MC6...MC9 because the calculations for MCP-1 have not been based on the direct temperature measurements in the IZ.

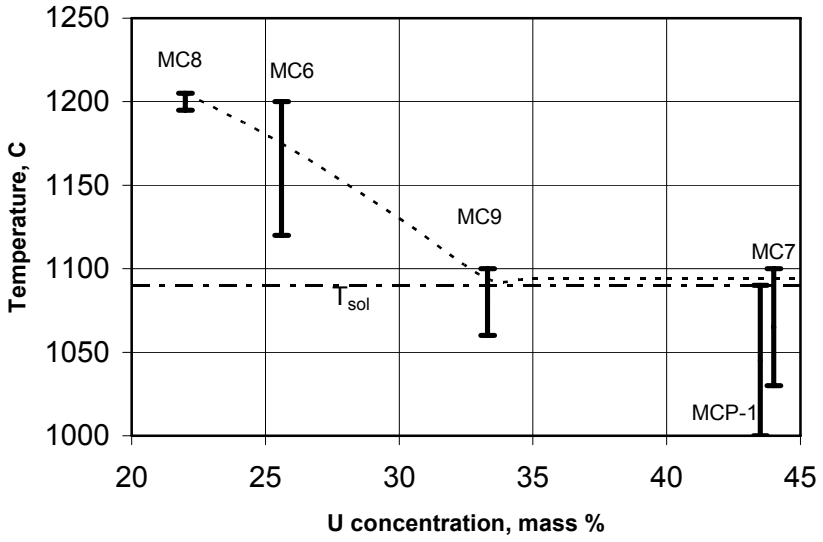

Fig. 3.3 – Temperature at the interaction zone boundary vs. U concentration

Thus, the results of MCP-1 and their main differences from the findings of MC6 should be explained rather by different degrees of molten corium oxidation than by different orientation of the interface surface. To verify this conclusion, the test with the vertically positioned specimen should be repeated with molten corium C-30 ensured in it and online measurements of the corrosion depth and temperature in the interaction zone provided.

Conclusions

1. MCP-1 test presented an experimental investigation of the interaction between suboxidized corium and a cooled cylindrical specimen of the VVER vessel steel with vertical positioning of the interaction interface. The initial charge composition with C-30 oxidation index corresponded to conditions of MC6 in which the interaction interface was positioned horizontally. Like in MC6, the regime of maintaining stationary thermal conditions lasted for 10 hours.
2. Posttest analyses have yielded the following results.
   - Similarly to all METCOR tests with suboxidized corium, the interaction zone (IZ) formed in the specimen body and contained large amounts of U and Zr, but their concentrations were significantly higher than in MC6.
   - The maximum specimen surface temperature (below the crust) amounted to approximately 1435°C at the heat flux from the melt of about 2.0 MW/m^2. These values exceed the corresponding ones in MC6.
   - The temperature boundary of the zone of interaction with the specimen is around 1000...1090°C. It corresponds to this parameter minimum value determined in MC7, MC9, and is about 100°C below the value from MC6.
   - At the melt surface, there was a thick crust with a composition differing from that of the melt. As a result, the index of melt oxidation was significantly lower than that of the initial charge and equaled C-17.
   - The corium ingot was discovered to contain a compact metallic body with U and Zr concentrations exceeding the respective average figures for the IZ.
   - In contrast to MC6, the incubation period was short or absent at all.
3. The analysis of the obtained results and those from MC6...MC9 and MASCA yields the following conclusions:
   - A significant reduction of the melt oxidation index resulted from the increased concentrations of U and Zr in the IZ in comparison with MC6.
   - A decreased (compared to MC6) final temperature boundary between the IZ and steel specimen is due to a higher (compared to MC6) U and Zr concentration in the IZ.
   - A considerable shortening of the incubation period in comparison with MC6 may be due to a higher temperature on the steel specimen surface and a higher the heat flux from the melt to the specimen.
   - Therefore, the main differences in the results of MCP-1 and MC6 are deemed not be related to the interface surface orientation. Verification of this conclusion requires a special test.

References

1. S.V. Bechta et al. New Experimental Results on the Interaction of Molten Corium with Reactor Vessel Steel, 2004 ICAPP′04, Paper 4114.
2. Yeremina B.G. Gas analysis. Moscow, Mir Publishers. 1955. (Rus.)
3. Baksanova L.E., Budnikov V.I., Valtsifer V.A. Gas volumetric method of active aluminium determination in polymeric materials. Factory laboratory. No.7, Vol. 66. 2000. (Rus.)
4. GOST 12365-84. Alloy and high-alloy steels. Methods of zirconium determination. (Rus.)
5. Yelinson S.V., Nezhnova T.I. Photometric determination of zirconium in niobium and other metals // Factory laboratory. Vol. 30, No.4, 1964. p. 396-399 (Rus.)
6. Goryushina V.G., Romanova E.V., Archakova T.A. Colorimetric methods of zirconium determination in alloys // Factory laboratory. Vol. 27, No.7, 1961. p. 795-797 (Rus.)
7. Riabchikov D.I., Seniavin M.M. Analytical chemistry of uranium. Moscow, Publishing House of the USSR Academy of Sciences. 1962. (Rus.)
8. Lukianov V.F., Savin S.B., Nikolskaya I.V. Photometric detection of uranium microquantities using reagent arsenazo III. JACh., v. XV, issue 3. 1960. (Rus.)
9. Markov V. K. et al. Uranium. Methods of its determination. Moscow, Atomizdat Publishers, 1964. (Rus.)
10. GOST 4011-72. Drinking water. Methods for determination of total iron. (Rus.)
11. Sendel E. Methods of metal traces determination by colorimetry. Moscow, Mir Publishers, 1964. (Rus.)
12. M. Bekkert and H. Clemm, Methods of Metallographic Etching: A Handbook [Russian translation], 2nd ed., revised and corrected. Moscow, Metallurgiya Publishers, 1988, 400 p.
13. Gulyaev A.P. Metal science. Metallurgiya Publishers, Moscow, 1977 (Rus.).
14. Heat treatment in mechanical engineering: Reference Book / Ed. Yu.M. Lakhtin, A.G. Rakhshtadt. Moscow, Mashinostroyenie Publishers, 1980, 783 p. (Rus.)
15. M. Barrachin, F. Defoort, Thermophysical properties of in-vessel corium: MASCA program related results, Proceedings of MASCA Seminar 2004, Aix-en-Provance, France, (2004).
16. S.V. Bechta et al. Experimental Study of Interactions Between the Suboxidized Corium and Reactor Vessel Steel. 2006. ICAPP′06, Paper 6054.